UNIVERSIDADE DE LISBOA

FACULDADE DE CIÊNCIAS

DEPARTAMENTO DE FÍSICA

Whole-Brain Mapping of Cerebrospinal Fluid Velocity and Displacement Over the Cardiac Cycle using Phase Contrast MRI and Optimization of a DENSE Sequence.

Francisco Martins Prata Fonseca Sousa

Mestrado Integrado em Engenharia Biomédica e Biofísica

Perfil em Sinais e Imagens Médicas

Dissertação orientada por:
Dr. Jaco Zwanenburg, University Medical Center Utrecht
Prof. Dr. Alexandre Andrade, Faculdade de Ciências da Universidade de Lisboa

2021

All we have to decide is what to do with the time that is given us.

J.R.R. Tolkien

Acknowledgments

Writing a dissertation is a weary and troublesome process that could never be completed without the support and love of the people that surrounding, especially in a year so strange as 2020. Putting into words, the gratitude I feel would always fall short of expectations. Nevertheless, here is my best and honest attempt.

First of all, this project would never see the light of day if not for the willingness of Dr. Jaco Zwanenburg to receive me in UMC Utrecht and to greet me with open arms. His guidance was nothing short of spectacular as I always felt a sense of purpose and direction in my work.

To Jacob-Jan, whose endurance to my questions, doubts, and general lack of knowledge can only be described as herculean. My sincere thanks for all the patience and valuable lessons.

To Ayhan, without you, the imaging world would definitely be a darker place. Thank you for all those night walks, discussing the sometimes overcomplex imaging world.

I would also like to express my gratitude towards the Erasmus+ institution for the support throughout my stay in Utrecht.

The last six years spent in university were filled with unforgettable moments that I'll cherish throughout my all life. My academic path allowed me to meet amazing people and create friendships that made all this journey worthwhile. It's impossible to name all of them, but there are some that I can't avoid but mention here.

Firstly, I would like to thank all professors in IBEB, but especially to my internal supervisor Professor Alexandre Andrade for his guidance throughout this project and during all my journey at Faculdade de Ciências.

To José Nuno Teixeira, my fake "godfather" and DnD introducer. When I was 18 no person on the entire University campus seemed as wise as he was, and his tricks and tips were essential to me.

To João Campagnolo, my Benfica and tennis mate, group project companion, and mythical 20 at MMC, I can only thank for all the help and lessons he shared with me.

To Beatriz Padrela, a friendship founded on our common love for movies, coffee breaks, and philosophical debates that could last for a night.

To Inês Fragoeiro, the best housemate one could ask for. Without her and her extensive notes on all courses, I could have never finished my degree, and for that, I'm eternally grateful.

To Beatriz Gouveia, six years of countless adventures, parties, late talks, and a friendship that I'll carry with me forever. Housemates in London and Utrecht, Bia put up with all my jokes and neurosis with a smile on her face, and I returned that by listening to hours and hours of her singing.

To Flip, Johnny, Neto, Nuno, Manu, Pagou, Sajjad, Tiggy, and Xico, dearest of friends, companions during this journey and throughout the last ten years of my life. They had to put up with all sorts of things and always had nothing but unlimited love and friendship. I'm happy we grew as people and as friends together. A true fellowship.

To my grandparents, who have always been my role models ever since I was a child. Their love and guidance have always been foundational for me. They have given me everything I could have asked for, and I always act so I can live up to their expectations.

To João, my brother, one of my best friends, creator of the best playlists to work to, he can always put me in the best or worst mood in a matter of seconds, but I wouldn't trade it for the world.

And finally, to my parents, who allowed for all this adventure to happen. Without their guidance, love, friendship, unlimited support, I would have been a completely different person. I hope that one day I can make them as proud as they make me every day.

Abstract

Cerebrospinal fluid (CSF) plays an essential role in the drainage of cerebral waste, and its continuous motion is vital to maintain the brain's homeostasis. Variations in this motion, associated with aging and disease, are observed in physical and physiological disorders, such as Alzheimer's Disease. Therefore, a deep understating of this fluid motion, such as its velocity and displacement, is fundamental to strengthen our knowledge of these diseases and might be vital to their prevention and treatment. Despite previous studies reporting CSF velocity and displacement using magnetic resonance imaging techniques, a complete picture of this fluid motion has not yet been obtained.

The aim of this study was to, first and foremost, obtain a general picture of CSF velocity and displacement using Phase Contrast (PC) MRI, a method of reference for velocity acquisition. Furthermore, this sequence was also used to optimize the parameters for an MRI technique called Displacement Encoding with Stimulated Echoes (DENSE), a sequence that was modified in order to be capable of measuring small displacements.

Four healthy subjects were studied using whole-brain ultra-high field (UHF) MRI at 7 Tesla (T). The volunteers were scanned using two different MRI imaging sequences: Phase Contrast MRI at 1 mm isotropic resolution and 3D T_1-weighted (T_1w) at 1 mm isotropic resolution. Additionally, two healthy subjects were scanned using PC and four different DENSE acquisitions. Firstly, two basic DENSE sequences with 2mm and 3mm isotropic resolution were acquired. Next, a DENSE acquisition with a T_2 prepared magnetization, and a DENSE sequence with a long echo time were acquired to avoid confounding effects from partial volume between tissue and CSF. The image processing pipeline included coregistration, segmentation, eddy current correction. Moreover, mean velocity and displacement maps were calculated for regions of interest previously selected.

The results in this study obtained from the PC acquisitions show consistent velocity and displacement values across all subjects. Furthermore, CSF shows higher values for the ventricular regions, such as the aqueduct, and predominant motion in the anterior and feet direction. Comparatively, regions in the periphery of the brain display slower velocities and smaller displacements. The displacement values obtained with PC were used to optimize the displacement sensitivity used in the DENSE acquisition. The DENSE sequence acquired with a T_2 magnetization preparation showed the most consistent results when compared to the Phase Contrast.

In conclusion, this project managed to study and quantify CSF behavior in the brain, which allows for the optimization of future sequences that desire a more detailed study of this fluid's in specific brain regions.

Keywords: cerebrospinal fluid, velocity, displacement, Phase Contrast MRI, DENSE.

Resumo

O líquido cefalorraquidiano (LCR) tem um papel essencial na drenagem dos resíduos resultantes do metabolismo cerebral e o constante movimento a que este fluido está sujeito é vital para manter a homeostasia do cérebro. Com feito, alterações neste movimento, geralmente associadas com o envelhecimento ou com doença, levam a perturbações fisiológicas, como a doença de Alzheimer ou a hidrocefalia. Por esta razão, é fundamental consolidar e aprofundar o conhecimento referente a este fluido, nomeadamente perceber como varia a sua velocidade e deslocamento, pois só desta forma será possível desenvolver e aperfeiçoar a prevenção e tratamento destas perturbações. Com efeito, este fluido está em constante movimento e o seu comportamento está intimamente ligado ao ciclo cardíaco. Apesar de estudos anteriores sobre a velocidade e o deslocamento do líquido cefalorraquidiano através de métodos de Ressonância Magnética (RM), ainda não existe uma descrição completa sobre o comportamento deste fluido.

O objetivo principal deste estudo, consistiu em obter uma descrição detalhada da velocidade e do deslocamento do LCR através da aquisição de imagens de ressonância magnética obtidas com contraste de fase, um método de referência no que toca ao estudo da velocidade de fluidos

No entanto, utilizar RM de contraste de fase para adquirir velocidades mais baixas, como as do LCR, requer tempos de aquisição mais longos e, consequentemente, as imagens obtidas estão mais sujeitas a distorções. Assim, a segunda parte deste projecto partiu dos resultados de deslocamento obtidos através da RM com contraste de fase para otimizar os parâmetros de uma segunda sequência de MR. Esta sequência é relativamente recente e possibilita o estudo do deslocamento sub-milimétrico do LCR associado ao movimento do cérebro através da aplicação de gradientes sucessivos (DENSE). Porém, é necessária uma escolha rigorosa dos parâmetros utilizados de forma a obter resultados que retratem o deslocamento do LCR de uma forma rigorosa e exata.

Na primeira parte deste projecto, quatro voluntários foram estudados utilizando RM com contraste de fase, entre outubro de 2019 e fevereiro de 2020, em concordância com as diretrizes éticas da *University Medical Center* em Utrecth, Países Baixos. As aquisições foram realizadas utilizando um *scanner* de RM Philips 7 T e dois tipos de contraste foram utilizados: contraste de fase com 1mm de resolução isotrópica e com uma codificação de velocidade de 5m/s, e imagens 3D com ponderação em T_1 com 1mm de resolução isotrópica. As imagens foram obtidas para três orientações distintas: anterior-posterior, inferior-superior, e direita-esquerda. Na segunda parte deste projecto, dois voluntários foram estudados, de janeiro a fevereiro de 2020, utilizando seis contrastes: contraste de fase com 1mm de resolução isotrópica, e imagens 3D com ponderação em T_1 com 1mm de resolução isotrópica, uma sequência básica DENSE com 2mm de resolução isotrópica, uma sequência básica DENSE com 3mm de resolução isotrópica, uma sequência DENSE com uma preparação T_2 com 3mm de resolução isotrópica e, finalmente, uma sequência DENSE com tempo de eco prolongado com 3mm de resolução isotrópica. No entanto, e ao contrário das imagens adquiridas na primeira parte deste projecto, as imagens da segunda parte foram obtidas apenas para a orientação inferior-superior. Todas as imagens adquiridas no decorrer desta dissertação foram obtidas com *gating* cardíaco. O *gating* cardíaco foi realizado através da utilização de um eletrocardiograma e de um oxímetro de pulso de modo a relacionar o evolução da velocidade e do deslocamento com o ciclo cardíaco.

Neste projecto foi também desenvolvida uma *pipeline* que permite que a partir das imagens adquiridas seja possível estudar a velocidade e o deslocamento do LCR. Esta *pipeline* inclui diversos passos. O primeiro passo consistiu em realinhar e co-registar as imagens obtidas de forma a permitir

uma análise voxel a voxel. Seguidamente, as imagens foram segmentas em três tipos de tecidos: LCR, substância cinzenta, e substância branca. Adicionalmente, as primeiras etapas foram realizadas através da utilização de *toolboxs* disponíveis no MATLAB como o SPM e o CAT12. Posteriormente, os artefactos presentes nas imagens, tais como as correntes-*eddy*, foram corrigidos. No decorrer deste projecto diversas regiões foram analisadas e foram divididas em dois grupos: regiões do sistema ventricular, nas quais se incluíram os ventrículos laterais, o terceiro e quarto ventrículo, o aqueduto de Sylvius e a Cisterna Magna; e regiões mais abrangentes, como a região anterior e posterior do cérebro. Estas áreas do cérebro foram selecionadas através da segmentação das imagens anatómicas. Finalmente, a velocidade de cada uma destas regiões foi extraída e integrada ao longo do ciclo cardíaco de maneira a calcular o deslocamento do LCR.

Os resultados obtidos relativamente à velocidade mostraram consistência para os quatro voluntários deste projecto. Verificou-se que as regiões do sistema ventricular demonstram valores de velocidade consideravelmente mais elevados do que as regiões mais abrangentes. Com efeito, a região que apresentou valores absolutos de velocidade mais elevados foi o aqueducto de Sylvius. Adicionalmente, verificou-se que as velocidades são superiores na orientação caudal-cranial e inferiores na orientação direita-esquerda. Concluiu-se também que o valor de velocidade escolhido não foi o mais indicado para as regiões mais abrangentes pois a velocidade destas regiões é significativamente inferior e, desta forma, poderá ter existido perda de sinal do LCR. Posteriormente, ao integrar a velocidade obtida através da RM com contraste fase obtiveram-se mapas de deslocamento para as mesmas regiões cerebrais. Estes resultados mostraram-se consistentes e, tal como anteriormente observado, o deslocamento é consideravelmente superior para as regiões do sistema ventricular. A região inferior do cérebro foi a que apresentou valores de deslocamento mais elevados, o que pode ser justificado pelo facto desta região se encontrar mais próxima do coração e, desta maneira, o LCR ser ejetado das regiões que ocupa com maior velocidade. Adicionalmente, verificou-se que as maiores alterações do deslocamento ocorrem imediatamente após a sístole cardíaca. Seguidamente, foi possível, a partir dos valores de deslocamento obtidos, determinar um valor ótimo para a sensibilidade, relativamente ao deslocamento, da sequência DENSE. Contrariamente à primeira parte deste projecto, os resultados obtidos utilizando as sequências DENSE dizem respeito exclusivamente às regiões mais abrangentes. De facto, esta exclusão das regiões do sistema ventricular foi causada pela baixa resolução das imagens obtidas que, desta forma, não permitiram uma segmentação de áreas tão reduzidas com fiabilidade razoável. Os resultados desta análise mostram que a sequência utilizada cujos resultados de deslocamento se assemelham mais aos resultados obtidos através do contraste de fase foi a sequência que utilizou a preparação T_2. Por oposição, as sequências básicas utilizadas mostraram semelhança reduzida com o método de comparação. Esta diferença observada foi justifica pela baixa resolução das imagens adquiridas, o que contribui para que não fosse possível eliminar o efeito de volume parcial. Adicionalmente, concluiu-se que o valor de sensibilidade para o deslocamento utilizado não foi o correto para estas regiões e, desta forma, houve perda de sinal adquirido justificando assim às diferenças encontradas entre os dois métodos.

Concluindo, esta dissertação cumpriu o objetivo principal proposto, nomeadamente fazer uma descrição completa e quantificar a evolução da velocidade e do deslocamento do líquido cefalorraquidiano ao longo do ciclo cardíaco. Adicionalmente, o método de RM com contraste de fase mostrou ser um método fiável para o estudo do comportamento do LCR mesmo em regiões com velocidades mais lentas. Os resultados de deslocamento obtidos através da utilização do método DENSE permitiram confirmar o potencial desta técnica para medir deslocamentos sub-milimétricos. No entanto, este método ainda necessita de ser otimizado de forma a ser uma alternativa viável ao contraste de fase. Finalmente, os resultados obtidos neste estudo permitem que estudos futuros utilizem os valores máximos de cada região obtida de forma a otimizar futuras sequências.

Palavras-chave: líquido cefalorraquidiano, velocidade, deslocamento, RM com contraste de fase, DENSE

Table of Contents

List of Figures

List of Tables

List of Abbreviations and Notations

AP	Anterior-to-Posterior
CAT	Computational Anatomy Toolbox
CNR	Contrast-to-Noise Ratio
CSF	Cerebrospinal Fluid
CP	Choroid Plexus
DENSE	Displacement Encoding via Stimulated Echoes
ECG	Electrocardiogram
FCUL	Faculdade de Ciências da Universidade de Lisboa
FH	Feet-to-Head
FID	Free Induction Decay
fMRI	Functional Magnetic Resonance Imaging
FOV	Field-of-View
G_{enc}	Gradient Encoding
GRE	Gradient Echo
GM	Gray Matter
MATLAB	Matrix Laboratory
MR	Magnetic Resonance
MRI	Magnetic Resonance Imaging
PC	Phase Contrast
PPU	Peripheral Pulse Unit
RF	Radiofrequency
RL	Right-to-Left
ROI	Region of Interest
SE	Spin Echo
SNR	Signal-to-Noise Ratio
SPM	Statistical Parametric Mapping
T	Tesla
TE	Time of Echo
TM	Mixing Time
TR	Time of Repetition
T1w	T1-weighted
T2w	T2-weighted
UHF	Ultra-High Field
V_{enc}	Velocity Encoding
WM	White Matter
3D	Three Dimensions

1. Introduction

The evolution of our species has been tightly connected to the development of one of the most complex organs in our anatomy, the brain. Throughout history, we have tried to study and understand this organ, and even though our knowledge of brain anatomy and function has exponentially increased, there is still a wide information gap that remains to unveil.

Simultaneously, the prevalence of neurodegenerative diseases, such as Alzheimer's disease and Parkinson's disease, has been increasing due to the increase in average life expectancy [1]. Therefore, a wide range of fields such as Neurosciences, Biochemistry, Medicine, among others, have switched some of their attention to this particular organ to better grasp what leads to these disorders and, consequently, develop new treatments.

The human organism has several ways to provide its organs with the vital nutrients needed for the different metabolism processes, *e.g.*, the circulatory system and the lymphatic system. Moreover, these systems are also responsible for eliminating and excreting toxins that result from these metabolisms. However, the brain is a complex system that possesses its own circulatory system that works in cooperation with the systems mentioned above in order to maintain its homeostasis.

Cerebrospinal fluid is a fluid with a pivotal role in our organism [2]. In fact, CSF is a fluid that is continuously in motion to provide the brain with essential substances that keep its homeostasis. Moreover, CSF motion provides a way for clearance when it comes to unnecessary substances. As a result, a considerable number of hypotheses have linked disturbances in CSF dynamics to physical conditions such as hydrocephalus and physiological disorders like dementia and Alzheimer's disease [3]. Therefore, the study of cerebrospinal fluid dynamics in the healthy and unhealthy brain is pivotal to not only understand the relationship between CSF and these disorders but also to strengthen our knowledge of these diseases and better prevent, diagnose, and treat them.

The studies regarding CSF dynamics have been steadily increasing in the last decades. The aim of these studies is to develop non-invasive methods capable of assessing this fluid behavior. Furthermore, it is necessary to understand the different aspects that influence CSF velocity, flow, and displacement and quantify them in different brain regions. Although new techniques that allow for this assessment have emerged, there is still a long way to go in terms of validation of these techniques. There is still a wide knowledge gap in this field, regarding the size and direction of net CSF flow in the ventricles and inside the brain and regarding where it is produced [4].

The objective of this project is, first and foremost, to quantify and describe both the velocity and displacement of CSF in the human brain using Ultra High-Field Phase Contrast Magnetic Resonance Imaging data. Secondly, the results obtained in this project are used to outline the parameters for an MRI technique, called Displacement Encoding with Stimulated Echoes, that was modified in order to study CSF displacement.

This project is part of the integrated BSc/MSc in Biomedical Engineering and Biophysics of Faculdade de Ciências da Universidade de Lisboa (FCUL). The research described in this dissertation was carried out at UMC Utrecht between September 2019 and March 2020. While the research in the UMC was abruptly terminated due to the COVID-19 pandemic, the remaining work was carried in Portugal from March 2020 to September 2020. Besides the processing of MRI data, the development of an image processing pipeline for its study, and the analysis of the results, there was involvement in the acquisition of all analysed data. These additional tasks enabled a closer contact with the scanner

itself, pivotal in order to get a better understanding of the sequences used. The work developed was supervised by Associate Professor Jaco M. Zwanenburg (UMC Utrecht) and Assistant Professor Alexandre Andrade (FCUL) and co-supervised by PhD Student Jacob-Jan Sloots (UMC Utrecht).

This dissertation is divided into six different chapters. **Chapter 2** provides a theoretical background to this project. **Chapter 3** comprises an examination of the methodology that was adopted throughout this project. This project's results are displayed in **Chapter 4** and are addressed and discussed in **Chapter 5**. Finally, **Chapter 6** concludes this project by providing some final remarks and future work.

2. Background

In this chapter, the theoretical framework of this dissertation is provided. Firstly, in **Section 2.1**, a brief introduction to cerebrospinal fluid is provided, particularly its characteristics, role, and anatomy. Then, **Section 2.2** consists of a description of CSF motion and the influence that both the cardiac and respiratory cycles have on its circulation. In **Section 2.3**, the principles of MRI and an overview of ultra-high field MRI are described. Next, **Section 2.4** presents a brief description of some important aspects of the MR image processing pipeline. Finally, **Section 2.5** provides an insight into the standard MRI sequences that acquire and analyse CSF motion.

2.1. Cerebrospinal Fluid: characteristics, role and anatomy

CSF is mainly composed of water, ions, vitamins, and peptides [2]. The traditional understanding of CSF physiology assumes that 80% of this fluid is secreted by the choroid plexus (CP) into the ventricular cavities while the remaining CSF is produced in other structures such as the brain parenchyma. In 1925, Harvey Cushing not only identified the CP as the primary source of CSF but also that the bulk flow of CSF runs through the ventricular system [4]. Moreover, the rate of CSF formation in humans is considered to range between 0.3 and 0.4 ml min^{-1} [5]. Additionally, the exit of CSF is conducted through the Foramen of Luschka and Magendie, which correspond to the fourth ventricle, into the subarachnoid space with subsequent absorption into the venous blood [2]. This process is also known as "third circulation" in opposition to the blood and lymph circulation (**Figure 2.1**).

Due to the work proposed by Stern and Gautier, in 1922 [6], CSF became considered a "nourishing liquor" as this fluid contains essential substances that penetrate the brain from CSF and that are essential to it. As CSF is continuously in motion, maintaining communication among the brain, spinal cord, nervous system, and lymphatic and vascular systems [7,8], CSF has a pivotal role, both physically and

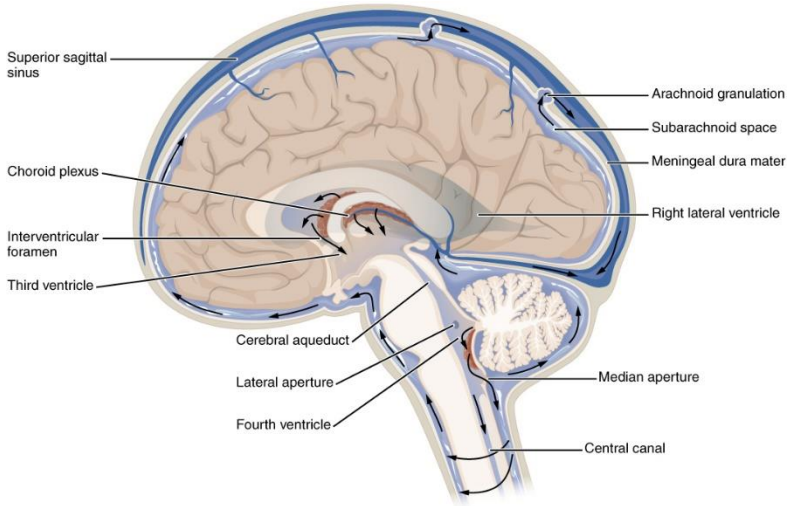

Figure 2.1: Cerebrospinal fluid circulation represented in a sagittal view [9].

physiologically. As for the first, CSF transmits vascular pulsation, buffers excessive brain pulsation, and has a buffer and buoyancy effect against external forces. Regarding physiology, this fluid is responsible for draining unnecessary substances (such as β-amyloid) from the brain parenchyma; substance exchange between the brain parenchyma, spinal cord, and nervous system [10-12]. Therefore, in order to fulfil these functions, CSF needs to be in constant motion.

However, ageing leads to a decline in CSF production and CSF flow [13], which may be due to age-related cognitive decline [14]. This decline in CSF clearance leads to the accumulation of protein aggregation and peroxidation products [15]. Furthermore, these accumulations contribute to brain diseases such as dementia.

2.2. CSF motion with respiratory and cardiac cycles

The first MRI study that showed that CSF velocity is driven by vascular pulsations was conducted in 1987 [16]. In fact, before this study, the popular belief was that the pulsatile force behind CSF motion was the expansion of the choroid plexus. Since then, several studies have confirmed that it is, in fact, the vascular pulsations that are responsible for CSF motion [17,18].

Therefore, CSF is not static as it exhibits pulsatile motion inside the ventricular system and between the cranial vault and spinal compartments, superimposed by bulk flow due to the renewed CSF and final clearance into the venous system [19]. This pulsatile pattern is essential to normal brain function, and several diseases manifest disturbances of CSF flow dynamics. CSF motion is thought to be composed of two components: cardiac-driven motion and a respiratory-driven motion [20]. Changes in blood volume caused by the cardiac and respiratory cycle lead to subtle brain tissue deformations. In fact, the variation of blood pressure in the brain's vessels leads to their swell and stretch, resulting in the displacement of the surrounding tissue [21].

The brain and the heart are intrinsically connected. During the normal cardiac cycle, approximately 750 mL of blood is pumped into the head per minute [22]. This relation results in a pulsatile viscoelastic deformation and volumetric strain of the brain tissue over the cardiac cycle. Imaging studies [19] have shown that the cardiac cycle dictates its pulsatile pattern onto the CSF, *i.e.*, the rise of the intravascular blood volume during systole leads to the swell of small brain vessels, which results in the expansion of the cerebral tissue towards the ventricles. The Monroe-Kellie doctrine states that there is a fixed intracranial volume, as the cranial vault is enclosed by ossified bones, which means that the CSF is pushed out of the brain into the CSF spaces towards the spinal canal to compensate for the additional blood volume [23]. This ejection of CSF to accommodate the expanded arteries during the systolic inflow of blood accounts for approximately 50% of the increase in intracerebral blood volume [24]. Moreover, the remaining 50% is accommodated by venous compression. Additionally, as the blood exits the brain during diastole, the vessels relax, and CSF returns.

More recently, several studies have investigated that CSF flow is influenced by respiration, *i.g*, Yamada et al. [25] found cranial CSF motion during inspiration and caudal CSF motion during expiration. Similarly, Dreha-Kulaczewski performed real-time CSF flow dynamics measurements and found upward CSF flow during inspiration and downward flow during expiration [26].

The influence that respiration has on CSF movement can be explained by the respiration cycles, which induce variations in thoracic pressure causing variations in the pressure of veins around the thoracic vertebral column. During inspiration, a drop in thoracic pressure occurs, which results in increased outflow of venous blood from the head [27]. Alternatively, during expiration, the thoracic pressure increases, resulting in a reduced outflow of venous blood from the head.

These variations in blood flow lead to alterations to the CSF flow, similar to the cardiac cycle's influence. Finally, even though CSF also has a bulk flow caused by new production and reabsorption, it is small compared to its pulsatile component [19]. In fact, while the average CSF net flow in the cerebral aqueduct ranges between 0.26-0.74 mL/min [27], the heartbeat induced stroke volume is approximately 1 mL/sec [27].

2.3. Magnetic Resonance Imaging

2.3.1. Principles of MRI

Magnetic Resonance Imaging is a medical tool well established for the past decades due to its excellent contrast potential and accuracy for most human tissues. In fact, MRI relies on the magnetic properties of tissues to produce an image. Generally, this technique uses the hydrogen nuclei (or the phosphorus nucleus), which is abundant in the human organism and can be found both in water and fat molecules. The proton's spin generates a magnetic moment that interacts with magnetic fields. The application of a strong, external magnetic field (B_0) aligns the nucleus to the external field [28]. Furthermore, this results in a precession movement around the direction of the magnetic field, which has a frequency proportional to the magnetic field strength and is expressed through the Larmor equation:

$$F = \gamma B_0 / 2\pi \qquad \text{(Equation 2.1)}$$

In which the precession frequency, F, is given by the product of the gyromagnetic ratio constant γ and the external magnetic field B_0, divided by 2π. Moreover, **equation 2.1** shows that all protons subject to the same magnetic field have the same Larmor frequency [29].

Using a radiofrequency (RF) pulse, it is possible to flip the magnetization of the body from a state in which it is parallel, net magnetization, M_Z, to the external magnetic field into the *xy* plane [30]. The magnetization in the xy plane is in an excited state because the protons accumulated energy from the RF pulse originating the free induction decay (FID) [30]. When the RF pulse ends, the protons relax, return to their initial state, and release the energy as an RF pulse. Consequentially, the magnitude of M_Z decreases over time and realigns along the *z*-axis. Moreover, the dephasing of the protons leads to the decreasing of the measured signal to zero and this process is called transverse relaxation. Furthermore, the transverse relaxation is mainly caused by the interaction between spins, called the spin-spin relaxation. The spin-spin relaxation explains the relaxation time T_2. In fact, the relaxation time is related to the loss of transverse magnetization through the following equation:

$$M_{xy} = M_0 e^{-t/T2} \qquad \text{(Equation 2.2)}$$

This dephasing effect is also caused by local field inhomogeneities, and these inhomogeneities are mainly caused by the main magnetic field inhomogeneity and by differences in magnetic susceptibility among different tissues [31]. The time associated with the dephasing caused by local field inhomogeneities is referred to as T_2^* relaxation.

Additionally, the longitudinal relaxation is caused by the interaction of protons with the surrounding tissue causes the loss of energy. This phenomenon is also called the spin-lattice relaxation, described by the relaxation time T_1, which refers to the time it takes for tissue to recover 63% of its original magnetization [32]. Similar to the loss of transverse magnetization, the recovery of the longitudinal magnetization is described in **equation 2.3**:

$$M_Z = M_0 \left(1 - e^{-\frac{t}{T_1}}\right) \qquad \text{(Equation 2.3)}$$

Different images and contrasts can be acquired in MRI by varying the pulse sequences and the parameters. Parameters such as the time of repetition (TR) that consists of the time between the application of an excitation pulse and the next pulse; and time of echo (TE), which is the time between the RF excitation and the peak measurement of the echo, lead do different acquisition protocols that allow for different imaging methods.

To create an MRI image, it is necessary to gather information regarding the location of the protons. In fact, this location requires the use of magnetic gradients, which change the magnetic field of each point within the MR imaging machine. Using three sets of coils, gradients can be applied in any orthogonal direction. Firstly, a gradient is used to select the image slice, which is defined by the frequency of the RF pulse. The two remaining gradients that encode for phase and frequency are then used to gather information regarding the individual pixel within a slice. The information for each pixel regarding phase and frequency is then stored in a matrix called *K-space* [33]. Using a mathematical algorithm called Fourier Transform it is possible to convert the raw data and reconstruct the image.

Finally, the handling of MR data also poses a significant challenge. MR imaging processing and analysis aim to improve the data quality and allow the extraction of information to be interpreted clinically and from a research perspective. MRI processes include several steps such as noise reduction, motion correction, coregistration, skull stripping, spatial smoothing, among others. Additionally, these steps provide a better quality of the data and, consequently, allow for a more robust analysis. Then, it is possible to analyse the data through different methods such as brain segmentation, subject registration, and the creation of regions of interest (ROIs) that can be analysed as a group.

2.3.2. Ultra-High Field MRI

Since the generalization of MR techniques in the 1970s for imaging purposes, several developments have arisen and change the use of this widespread imaging technique. One of the most prominent advances has been the increase of the external magnetic fields. While the majority of the clinical MRI scans are still being operated at low field (1.5T or below) [33], there has been a consistent increase in the magnetic field strength in neuroimaging centers located in hospitals and universities. In fact, in the last thirty years, the magnetic field strength has increased from 3.0 T to 9.4 T [34], and some research facilities have started to develop even higher fields such as 10.5 T and 14.0 T.

The increase of the magnetic field strength aims to push the boundaries of this technology by improving some of its parameters such as the sensitivity, contrast, and spatial resolution. One of the most important consequences of the increase of the field strength is the increase in the signal-to-noise ratio (SNR). Although it was considered, originally, that the SNR increased linearly with the magnetic field strength, it has been demonstrated that in the range of 3-9.4 T, it increases supralinearly [33]. The increase in this parameter, which broadly represents the measure of a true signal to noise, can be translated into higher spatial resolution or into higher temporal resolution. The spatial resolution improvement, for instance, is a great benefit as it allows for the detection of smaller features and for the mitigation of partial volume effect associated with smaller voxel sizes [33].

One of the most important aspects regarding the increase in the magnetic field strength refers to change in the relaxation times constants such as T_1, T_2, and T_2^*, as these constants depend on the field strength [31]. For higher fields, while the T_1 relaxation time for a certain tissue is increased, the T_2 and T_2^* decrease. This difference allows for an increase in the contrast-to-noise ratio (CNR) and, therefore, greater contrast between tissues, which proves to be one of the most important benefits of UHF for diagnostic imaging. In fact, the CNR increase contributes to more robust structural studies and Functional Magnetic Resonance Imaging (fMRI) studies.

Despite the several advantages granted by the increasing of the field, ultra-high field MRI has some drawbacks that must be considered when used. Firstly, an increase in the external magnetic field intensifies the physiological, transient side-effects such as dizziness, nausea, and metallic taste. Furthermore, higher magnetic fields might increase geometric distortions and intravoxel dephasing [35].

Additionally, acquisitions with higher spatial resolution are usually longer and, therefore, more sensitive to motion. This increase in motion sensitivity is also caused by the smaller voxel size [34].

All things considered, the benefits of UHF have proven to outweigh the challenges imposed by the increase of the magnetic field. Several MRI modalities have benefitted enormously from this increase in spatial resolution due to the increase in anatomical detail and precision. MRI. Additionally, the difference in the contrast behaviour has proven to be essential to several techniques such as fMRI.

2.4. MR Image Processing

2.4.1. Registration

To analyse neuroimaging data using a combination of different acquisition methods, it is pivotal to start with a series of spatial transformations. These transformations aim to reduce unwanted variance components in the voxels induced by movement and or by shape differences among series of scans. Voxel-based analysis relies on the assumption that data from a particular voxel belong to the brain's exact same region. If this assumption is not fulfilled, it leads to artifactual changes in the voxel values [36].

Image registration is a step in the imaging processing pipeline, which consists of geometrically aligning one image with another [37]. This process is a prerequisite for brain imaging applications that rely on comparisons between subjects, modalities, and even across time. Image registration allows the comparison between the values of two voxels in the two registered images, assuming that both voxels have the same coordinates. Furthermore, coregistration is a type of registration that spatially aligns different series of images belonging to the same subject with a reference image. The reference image is usually the first volume acquired or a template space. Coregistration can be used to align images from different MRI modalities and can also serve as a method to correct motion artifacts, such as random head movements.

Registration methods rely on transformation models, similarity measures, and optimization strategies. Furthermore, these methods can be divided into linear and non-linear depending on the deformations they perform. The former consists of transformation models that perform translations, scaling, and rotations. These linear methods deform the images but preserve collinearity and rations of distance. One particular case of a linear registration is the rigid-body transformation, which has six-degrees-of-freedom, as it only uses rotations and translations and is usually used in coregistration. 3D Rigid body transformations are characterized by three translations and three rotations on the three different axes [38]. As a result, each point in an image is described by three coordinates *(x1, x2, x3)* and *via* an affine transformation can be defined into the coordinates of another space *(y1, y2, y3).* This operation can be represented by a matrix multiplication, represented in equation 2.7:

$$\begin{vmatrix} y_1 \\ y_2 \\ y_3 \\ y_4 \end{vmatrix} = \begin{vmatrix} m_{11} & m_{12} & m_{13} & m_{14} \\ m_{21} & m_{22} & m_{23} & m_{24} \\ m_{31} & m_{32} & m_{33} & m_{34} \\ 0 & 0 & 0 & 1 \end{vmatrix} \qquad \text{(Equation 2.4)}$$

Conversely, non-linear models have higher degrees-of-freedom and warp the data to match both images.

2.4.2. Segmentation

The main aim of segmentation is to divide an image into several meaningful, homogenous, and nonoverlapping regions of similar attributes. The result of this process consists of an image of labels identifying each particular region or a set of contours that highlight each region's boundaries [39].

As stated previously, segmentation aims at dividing an image into different and meaningful regions. Therefore, it is critical to classify each region and assign each of these regions, or tissues, with specific values such as intensity, texture, and depth. In brain MRI, voxels are usually divided into three main types of tissues: gray matter (GM), white matter (WM), and CSF (**Figure 2.2**). Segmentation results have several uses that range from analysing anatomical structures to surgical planning.

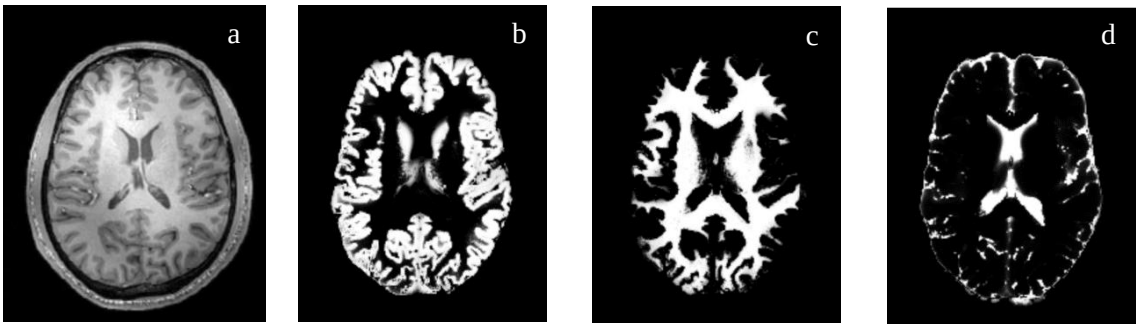

Figure 2.2: Axial slice obtained from a 7T MRI scan (a). Corresponding segmented tissues: Gray matter (b); White matter (c); CSF (d).

There are several segmentation methods, and these can be divided into intensity-based methods, atlas-based methods, surface-based methods, and hybrid segmentation methods.

2.4.3. Eddy Currents Correction

The three primary sources of inaccuracies in velocity images are eddy current effects, Maxwell terms, and gradient field nonlinearities [40]. Although concomitant field effects, also known as Maxwell terms, and spatial nonlinearity of gradients can be well approximated or modelled, the eddy current-induced velocity offset remains challenging to predict and account for [41].

Eddy Currents are the result of rapidly changing gradient magnetic fields that in turn induce stray currents in the surrounding conduction materials. These currents eventually generate their own magnetic field, opposing the original field [42]. Eddy currents induced in MRI systems through the application of pulsed magnetic-fields not only result in undesired, time-varying, magnetic-field gradient but also in magnetic field shifts. As a result, these gradients and field shifts lead to the appearance of artifacts like geometric distortions.

When it comes to PC-MRI, velocity images are affected by eddy currents, and this effect can be seen as it causes stationary tissue to display an apparent non-zero velocity, known as the background offset or baseline error. This may vary gradually with position over the velocity image and underlies stationary and moving tissues. Although typically small, it is important to address it as these calculations of volume flow are based on the summation of velocities through the whole cross-sectional areas of vessels and all phases of the cardiac cycle. Because of these two summations, the small background velocity offset error accumulates to give potentially significant errors [43].

Some methods allow for the compensation or even correction of these effects at their formation. Firstly, it is possible to pre-distort the gradient pulse so that the magnetic field generated by eddy

currents improves the original magnetic field. Secondly, by applying a secondary coil around the main gradient coil to reduce or cancel generated eddy currents, it results in an actively shielded gradient coil. Nevertheless, image shearing artifacts and image scaling artifacts can also be corrected *via* data post-processing.

One of the methods that allow for the correction of the background offset consists of using the apparent velocity values in stationary tissue close to the area of interest. In fact, this can be done by determining the offset in stationary tissue from the whole field-of-view and subtracting it from the original image [42]. However, this approach is limited by several requirements, such as sufficient stationary tissue at adequate SNR and avoidance of phase-encoded wraparound [43].

Another method that can be used, proposed by Chernobelsky et al. [44], consists of acquiring static phantom data from in vivo data and subsequently subtract it from the velocity data. Despite solving the problem of having enough stationary tissue, this method is time-consuming since it requires an additional phantom measure with identical imaging parameters.

Finally, it is also possible to use the magnitude data of a PC-MRI scan to create a mask of the stationary tissue and, consequently, calculate the linear offset caused by the eddy currents. As a result, this linear gradient is then subtracted from the velocity images, which generate a new velocity image free from eddy current artifacts. Nevertheless, this method relies on the assumption that the eddy current effect increases/decreases linearly from the origin point of each image.

2.5. In vivo quantification of Cerebrospinal Fluid Dynamics

2.5.1. Cerebrospinal Fluid Flow Dynamics

The movement of CSF within the brain has been studied since the early 1940s [45]. However, before the emergence of non-invasive MR techniques, invasive techniques, such as spinal puncture with the introduction of contrast, were the cornerstone of CSF flow dynamics [46,47]. Other methods included radionuclide and metrizamide cisternography infusion manometric tests and intracranial pressure monitoring [48]. In fact, the earliest evidence of CSF motion on MRI was the lack of signal observed in early studies, which was caused by sensitivity to oscillatory motion [49]. As the magnetic resonance signal sensitivity to motion became more widespread, phase-sensitive methods began to be applied, first, to blood flow by Grover and Singer [50]. Moreover, these new techniques lead the way to the proliferation of studies regarding CSF flow [51-55].

In fact, the first study to modify the phase imaging technique in order to allow for CSF flow quantification was proposed by J. P. Ridgway et al. in 1986 [52]. Additionally, this study concluded that the PC-MRI was able to demonstrate pulsatile CSF flow and, more importantly, that quantitative measurement of CSF velocity could be obtained with reasonable accuracy while assessing the direction of the flow. Nevertheless, this study was not able to quantify the velocity within the cerebral aqueduct.

The first study to quantify CSF flow inside the aqueduct was conducted in 1988 by Maschalchi M et al. [54]. Using cardiac-gated phase MR, the research was able to estimate CSF aqueduct velocities of 3-5 mm/s. Since then, most studies that quantify the flow of CSF have focused primarily on the aqueduct [56,57]. These studies serve different objectives, such as quantifying the flow for healthy and non-healthy subjects, assess whether the flow differs according to the anatomical location of the cerebral aqueduct that is used [58]. Furthermore, several studies take advantage of the advance of MR hardware and software to obtain images with higher spatial and temporal resolution and, consequently, to obtain more precise values for the CSF flow.

When it comes to mapping the CSF flow patterns within the human ventricular system, the number of studies is remarkably lower. The first study that tried to study CSF velocity profiles in order to define the CSF flow in ventricular and subarachnoid locations was carried out by Dieter R.Enzmann and Norbert J. Pelc in 1991 [59]. However, the first detailed demonstration of the behaviour of CSF was carried by Andreas Stadlbauer et al. in 2010 [60] Furthermore, some studies followed that quantified the CSF velocity in different brain areas such as the lateral ventricles, the Foramen of Monroe, the third ventricle, the aqueduct of Sylvius, and the fourth ventricle [61]. Nevertheless, these experiments were performed on 1.5 or 3 Tesla MRI scans, which do not possess the same resolution level as a 7T MRI scan.

There are several techniques capable of analysing this fluid's flow, and some of these techniques are described in the next sections of this dissertation.

2.5.2. MRI Acquisition of Cerebrospinal Fluid

CSF has a long T_1 and long T_2 values when compared to other tissues such as gray and white matter. Therefore, while it shows dark signals for T_1 weighted images (**Figure 2.3)**, it shows bright images for T_2-weighted images in MRI. Furthermore, T_2-weighted images are widely used for clinical diagnosis of CSF-related diseases such as hydrocephalus and aqueduct stenosis [62].

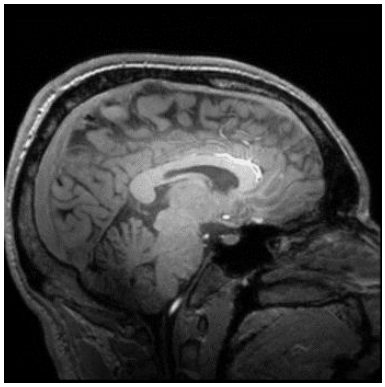

Figure 2.3: MRI scan acquired at 7 Tesla using T1w contrast. Tissues with long T_1's appear dark, such as CSF, and tissues with shorter T_1's appear in shades of grey, such as gray and white matter.

However, when it comes to CSF motion measurements it is necessary to use different imaging protocols. There are several techniques that make it possible to study CSF motion, such as Phase Contrast MRI, echo-planar imaging (EPI), time-spatial labelling inversion pulse (Time-SLIP), dynamic improved motion-sensitized driven-equilibrium steady-state free precession (dynamic iMSDE SSFP) [63-66]. Nevertheless, this work will focus primarily on Phase Contrast MRI since it is one of the most studied and documented techniques and on DENSE, a recently new technique able to quantify CSF displacement.

2.5.3. Phase Contrast MRI

As explained in the previous sections, the bulk of diagnostic MRI findings are based on signal amplitude in which the gray-scale display is based directly on the signal strength from a particular voxel. However, these signals retain information about their frequencies and phase, which are typically not used. The phase change of a proton can generate an image, on which the local phase shift can be used to display a map. Here, the voxel density is based directly on this phase shift instead of on the signal amplitude.

Phase Contrast MRI is a non-invasive technique that consists of applying sequentially two equal but opposite gradients, which causes stationary protons to have no phase shift. In fact, the first gradient causes a uniform phase shift [67]. Afterward, the opposite gradient is applied in order to remove the phase shift of the stationary protons and alters the phase of the protons moving in the direction of the gradient (**Figure 2.4**). Therefore, when the signal phases are deconstructed, only the moving protons have phase shift. Moreover, the higher the velocity of these protons, the greater the phase shift, which allows for the velocity to be mapped quantitatively.

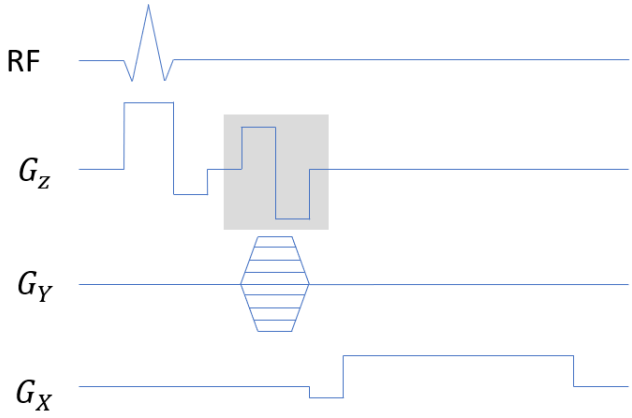

Figure 2.4: PC-MRI simplified pulse diagram. A bipolar gradient is applied along the direction of the flow (grey box). Z direction represents the direction of the image selection; G_Y is the phase-encoding direction; and G_X is the frequency encoding direction [67].

The degree of phase shift in PC-MRI is directly linked to the proton velocity in the direction of the gradient (**equation 2.5**). However, due to arithmetic limitations (i.e., at 360°, the measured angle wraps back around to 0º and continues forward), only a specific range of velocities can be mapped [68]. For instance, a phase shift of 405º is indistinguishable from a phase shift of 45º. Furthermore, as it is crucial to measure both the forward and backward direction, measured phase angles only range from -180° to 180°. If the angle measurements exceed in either direction, then aliasing artifacts occur.

$$\Delta\phi = \gamma\vec{v}\Delta M_1 \qquad \text{(Equation 2.5)}$$

Equation 2.5 represents the phase shift ($\Delta\phi$), where γ is the gyromagnetic ratio, $\vec{v}$ is the proton velocity, and ΔM_1 represents the change in the first moment of the velocity encoding gradients, *i.e.*, the difference between the two opposite scans [68]. Since magnetic moment change is proportional to the gradient strength, then the phase shift is also proportional to this gradient. Furthermore, since $\Delta\phi$ values must be within -180 an 180, **equation 2.5** can be rearranged into **equation 2.6**:

$$v_{enc} = \frac{\pi}{\gamma\Delta M_1} \qquad \text{(Equation 2.6)}$$

Therefore, for a given bipolar gradient, there is a maximal velocity that can be measured in order to avoid aliasing. This velocity is called the encoding velocity (V_{enc}). This velocity is inversely

proportional to the gradient strength [69]. As a result, V_{enc} is increased by decreasing the gradient strength and vice-versa. Nevertheless, this relation means that for slower velocities, the gradient strength needs to increase as well as the minimal repetition time TR which cannot be increased indefinitely.

Moreover, it is vital to know the approximate velocities to be measured in order to select the correct and most accurate V_{enc} for a Phase Contrast sequence. The selection of this value is pivotal as the underestimating of it leads to aliasing factors, and the overestimation leads to low phases accumulation, *i.e.*, the full dynamic range between $-\pi$ and $+\pi$ is not covered. Consequently, this results in low SNR. There is an extensive range of values that can be used as V_{enc}. For example, Phase Contrast imaging of the cerebral arterial vasculature requires a high V_{enc}, i.e., 70 cm/sec. However, a typical V_{enc} value for CSF traversing through the foramen magnum is 10cm/s, while for CSF traversing the aqueduct is 8cm/s [70,71].

Phase Contrast MRI allows for the estimation of different parameters such as mean and peak flow velocity, vessel compliance, tissue motion estimation, among others. PC-MRI sequences produce magnitude and phase images (**Figure 2.5**). In magnitude images, which represent the flow, stationary regions remain dark while regions that are moving are represented with different tonalities of grey to white. The phase image represents the flow direction, i.e., forward flows appear bright while backward flow appears dark.

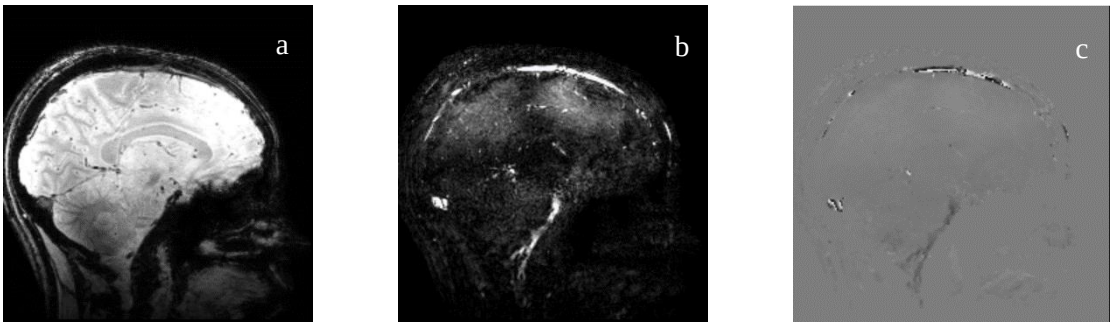

Figure 2.5: Phase Contrast Magnitude (a) and Phase Contrast modulus image (b) acquired at 7T MRI scan using Phase Contrast MRI. Velocity image map resulting from the PC scan (c).

It is possible to synchronize the PC-MRI acquisition with the cardiac cycle through cardiac gating. The cardiac gating enhances the sensitivity in pulsatile CSF measurements [72]. It can be performed with an electrocardiogram by two different methods: either prospective gating or retrospective gating. The first method triggers the image acquisition through the R wave. In prospective gating, the acquisition starts with the R wave of an electrocardiogram (ECG). Usually, this acquisition is finished before the next R wave in order to accurately detect the next trigger, which means that the entire cardiac cycle is not assessed [73]. In the second method, the data is acquired continuously throughout the cardiac cycle [74]. Retrospective gating allows for the acquisition of the full cardiac cycle as the electrocardiographic signal is acquired, and the data points are re-sorted retrospectively [73]. However, this method requires post-processing, such as interpolation methods, in order to retrospectively sort the data to it position on the RR interval [75]. These methods allow the study of the relation between velocity and the effect that the cardiac cycle has on it.

Like traditional MRI and other conventional imaging modalities, PC-MRI has some limitations and constraints. Firstly, whenever more dimensions of spatial, temporal, and velocity encoding are desired, the scan time can increase to be unfeasible. Furthermore, PC-MRI's velocity flow fields suffer from inaccuracies due to motion artifacts, and gradient-attributed phase errors, such as eddy currents, caused by the rapid change of the gradient magnetic field, which have to be accounted for [76]. Phase Contrast is also susceptible to partial volume effect, especially in voxels near the vessels. The partial volume

effect results in voxels containing information regarding both stationary and flowing tissue, which might contribute to CSF flow overestimation [77]. However, this can be mitigated through the increase of the spatial resolution. Moreover, manual segmentation methods such as manual regions of interest are responsible for inter-observer and intra-observer variability in the collected data as the size of the ROI affects stroke volume flow rate and mean velocity [69].

Phase Contrast MRI is a valuable technique to estimate CSF flow. When using PC-MRI, it is important to choose the velocity encoding value correctly. In fact, the maximum velocity set in V_{enc} should be equal or higher than CSF velocity in to avoid aliasing artifact but high enough to produce reasonable signals. A typical V_{enc} value for CSF traversing through the foramen magnum is 10cm/s while for CSF traversing the aqueduct is 8cm/s [78]. However, it may be necessary to adapt the V_{enc} values in the presence of pathological disorders, e.g., in aqueduct stenosis.

Nevertheless, compared to blood flow measures, CSF flow measurements are less accurate due to their intrinsic smaller magnitude and reversal flow direction. Additionally, CSF spaces also do not conform to the near-cylindrical shapes of cerebral blood vessels, which complicates the determination of perpendicular planes needed in volumetric flow measurements, making CSF quantification less precise [20].

Additionally, PC-MRI is more suited for encoding high velocities. Using PC-MRI to acquire slow velocities, such as CSF velocities, requires large velocity encoding gradients to be applied, even with state-of-the-art gradient systems. This results in longer TEs and TRs, which consequentially reflects on longer acquisition times and phase distortions [79]. These distortions are a direct consequence of eddy currents and Maxwell terms.

In conclusion, acquiring CSF velocities with MRI proves to be a challenge not only due to the extensive range of values that can be found across the brain but also due to the intrinsic PC-MRI physics.

2.5.4. Displacement Encoding via Stimulated Echoes

As stated in the previous section, analysing slow velocities using Phase Contrast MRI implies the use of strong gradients and large TR, which is not always feasible.

The DENSE sequence was first proposed by Anthony H. Aletras et al. in 1998 [79] in order to obtain high-resolution myocardial displacement maps. This sequence uses stimulated echoes to encode the displacement. When combining both the advantages of tagging and phase velocity maps methods, it is possible to measure both small and large displacements over long periods of time while maintaining high spatial resolution [80].

The DENSE sequence consists of a motion encoding and decoding part (**Figure 2.6**) [79]. The first part encodes the current tissue position in the longitudinal magnetization by an RF pulse followed by an encoding gradient, G_{enc}, which introduces phase distortion (G_5) [80]. Subsequently, another RF pulse is applied to preserve the magnetization along the longitudinal axis. After the mixing time (TM), where the displacement is encoded, a third RF pulse is applied to bring the magnetization onto the transverse plane. There, a second gradient pulse G_6 (where $G_5 = G_6$) rewounds phase distortion from the first lobe. If there is tissue displacement along the direction of these gradients, it is reflected on a phase shift in the resulting phase imaging.

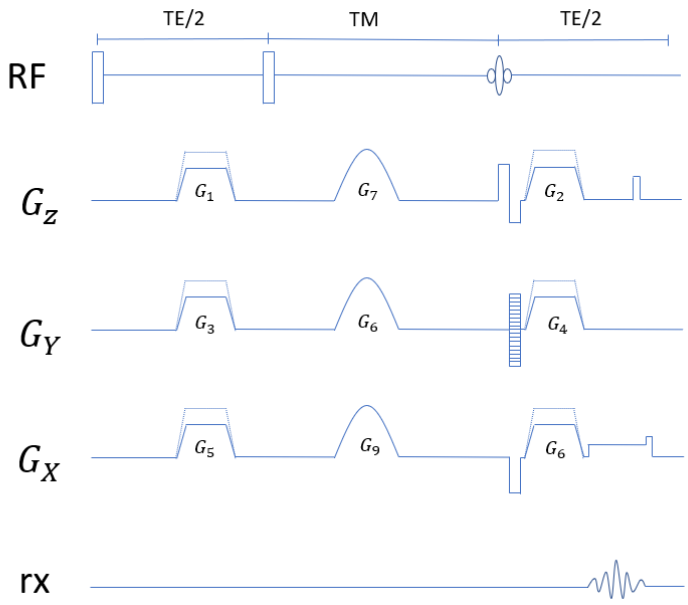

Figure 2.6: DENSE pulse sequence. Spin phase wrapping occurs through the application of gradient pulses G1, G3, and G5. The corresponding gradient pulses G2, G4, and G6 totally unwrap the phase for static tissue [79].

The encoding and decoding gradients alternate in sign every other dynamic in order to distinguish between the phase contributions due to motion and other cofounding phase contributions, e.g., static RF pulse, phase induced by off-resonance effects, and dynamic phase variation induced high respiration related B0 fluctuations [81]. The separating of the motion encoding and decoding gradients, using stimulated echoes, limits the effect of eddy currents as this effect results from rapidly changing the gradient magnetic fields. Furthermore, the fact that the gradients are separated in time, allows this technique to be more sensitive to smaller velocities without the use of impractical larger gradients [82] and without excessive prolongation of TRs and TEs [80].

The tag spacing T_{enc} in $mm/2\pi$ describes the sensitivity for the spatial displacement encoding of this sequence and relates to the SNR in the displacement maps. In **equation 2.7**, SNR_M is the SNR magnitude of the stimulated echo image. Furthermore, larger encoding gradients provide an increased displacement sensitivity (smaller T_{enc}). Furthermore, when multiplying T_{enc} by $\frac{\pi}{2}$ we obtained a parameter, similar to V_{enc} in PC-MRI, called D_{enc} that is given in mm, and represents the maximum displacement value that produces a phase wrap [21].

$$SNR_{\text{displ}} = \frac{d(t)}{T_{\text{enc}}} SNR_M \qquad \text{(Equation 2.7)}$$

Equation 2.7 shows that for higher displacement values, $d(t)$, a higher SNR ensues. Therefore, regions with higher velocities will eventually lead to higher displacements and, ultimately, to higher SNR. This means that regions that are expected to have higher displacements will provide reasonable

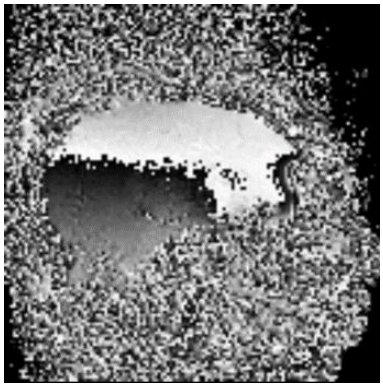

Figure 2.7: Sagittal slice obtained from an MRI scan acquired at 7 Tesla using DENSE sequence (Subject 1).

SNR values, while regions with smaller displacements might not produce useful images due to low SNR. In conclusion, it is critical to evaluate the range in which the CSF velocity and displacement varies, in order to understand how to optimize DENSE parameters to allow this technique to be used in a relevant way.

In 2009, Soellinger et al. [80], using the DENSE sequence, were able to assess the pulsatile brain motion down to displacement amplitudes of 10^{-2} mm. In fact, the cardiac-gated DENSE method was shown to be capable of capturing the displacement field maps over the cardiac cycle [83,84]. However, these data were acquired over several minutes, which prohibits to study the respiration-induced tissue motion and deformation. In a work from 2018 conducted by J.J. Sloots et al. [85], it was shown that DENSE allows for the separate assessment of cardiac- and respiration-induced motion.

The sequence used to tag brain motion is similar to the one shown in **Figure 2.6.** However, the parameters of the sequence, such as the tag spacing T_{enc}, and the flip angle, need to be changed in order to optimize the sequence for CSF acquisition. Choosing the correct T_{enc} is of pivotal importance as it allows to study the displacement in a particular area. Moreover, as the CSF displacement values vary from region to region, it is necessary to choose the region to analyse so that a proper T_{enc} can be chosen. For instance, while peak heart displacements can reach 1-2 cm, the peak displacements in some brain regions can be on the order of 1-2 mm or even smaller, which shows the importance of correctly choosing the right T_{enc}.

Additionally, there are some variations of this sequence that can be applied in order to get better SNR results or to avoid artifacts. The parameters used to acquire these sequences are detailed in **Section 3.1.2.**

3. Methodology

In **Chapter 3**, the methodology for this dissertation is provided. Firstly, **Section 3.1** addresses the recruitment of subjects for each acquisition as well as the parameters that were used in each acquisition performed in this project**. Section 3.2** describes the image processing pipeline used for both acquisitions. Next, **Section 3.3** explains which anatomical regions were selected and how the selection was performed. **Section 3.4** addresses the methodology used to obtain the velocity maps. Finally, **Section 3.5** delineates the creation of displacement maps related to both PC-MRI and DENSE.

3.1. Subject Recruitment and Data Acquisition

3.1.1. Subject Recruitment

Five healthy volunteers (three male, age range 21-29 years, average 24) participated in this study. The MRI data presented in this study was acquired between October 2019 and February 2020. Informed consent was given in accordance with the Institutional Review Board of the University Medical Center Utrecht (Utrecht, The Netherlands).

The volunteers were scanned 7T MRI (Philips Healthcare, Best, The Netherlands) using an 8-channel transmit and 32-channel receive head coil (Nova Medical, Wilmington, MA). The physiology was recorded using vendor supplied equipment: peripheral pulse unit (PPU) and electrocardiogram were used for cardiac gating. Furthermore, all scans were performed between 10:00 and 12:00.

3.1.2. Phase Contrast MRI

The first four subjects were scanned using Phase Contrast MRI. The PC-MRI acquisitions were performed with sagittal orientation and acquired with three different velocity encoding directions: Right-to-Left (RL), Feet-to-Head (FH), and Anterior-to-Posterior (AP).

For this part of the study, the subjects were scanned using two different MRI modalities: 3D-T_1w and PC-MRI. The imaging parameters for both sequences are presented in **Table 3.1**:

Table 3.1: Sequence Parameters for two MRI contrasts: 3D-T1-Weighted and Phase Contrast.

Contrast	3D-T_1w	PC
T_E (ms)	1.9	10.6
T_R (ms)	4.2	17.9
Inversion Delay	1.2	
Flip Angle (°)	5	9
FOV (mm)	288 x 288 x 190	224 x 224 x 180
Resolution (mm)	0.86 x 0.86 x 1	1 x 1 x 1
Avg. Acq. Time (min)	1.9	4.8
Cardiac Synchronisation	-	Retrospective
Cardiac Phases	-	11-18
Avg. Heart Rate	-	75
V_{enc} (cm/s)	-	5
Encoding Directions	-	FH, RL, AP

T_E – Time of Echo; T_R – Time of Repetition; FOV – Field of View; Avg. Acq. Time – Average Acquisition Time for each orientation; V_{enc} – Velocity Encoding; FH – Feet-Head; RL – Right-Left; AP – Anterior-Posterior.

3.1.3. DENSE

For this part of the study, two of the five subjects (Subject 4 and 5) were also scanned using four slightly different DENSE sequences, and their respective parameters are described in **Table 3.2**. For all the DENSE sequences presented in this work, the T_{enc} chosen was 1mm/2π. This value of sensitivity was chosen, bearing in mind the results obtained from the Phase Contrast acquisition, described in the previous section. Additionally, only the FH encoding direction was acquired. This decision was based in the fact that the aim of this project was to get a sense on what displacement sensitivity should be used in order to study CSF motion and, consequently, the FH orientation was chosen since it is the one where, according to the results obtained in **Section 4.2.2**, the biggest CSF displacement occurs.

Unlike the PC-MRI analysis, several DENSE acquisitions were performed in order to understand which one was the most suitable to analyse the displacement of CSF. Two DENSE basic sequences were acquired, only differing in their spatial resolution. The first is a basic DENSE sequence with 3mm isotropic resolution and the second with 2mm isotropic resolution. The low spatial resolution of these sequences leads to partial volume effect. In order to mitigate this phenomenon, two additional sequences were acquired. Both of these acquisitions used different strategies to eliminate the partial volume effect that is a direct consequence of the low spatial resolution.

The first one was a DENSE sequence that used a T_2 preparation. This means that a T_2-weighted magnetization-prepared sequence (T_2 Prep) was applied. This magnetization preparation is applied before the final RF excitation pulse and consists of a 90º block pulse, followed by two adiabatic (180º) refocusing pulses, and a -90º pulse that refocuses the magnetization (**Figure A.1**). This sequence was original proposed by Brittain et al. [87]. With this preparation, it is possible to saturate tissues with a short T_2, such as GM and WM, while having a minimal effect on CSF magnetization, which has a long T_2. The T_2 magnetization preparation allows, therefore, to mitigate the partial volume effect created by the low resolution with which these sequences were acquired.

The second DENSE sequence performed consists of applying a longer echo time than usual, which means that only tissues with a longer T_2 relaxation will retain the signal. Therefore, the long echo acquisition has a similar effect to the T_2 Prep in the sense that its objective consists of making the water the only tissue with signal. This sequence is called, in this project, Long Echo sequence.

Table 3.2: DENSE Sequence Parameters for four different contrasts.

Contrast	T2 Prep	Long Echo	Basic 3mm	Basic 2mm
TE (ms)	14	80	14	20
TR (ms)	1090.9	1090.9	1090.9	1090.9
Flip Angle (°)	90	90	90	90
FOV (mm)	180 x 250 x 250	180 x 250 x 250	180 x 250 x 250	180 x 250 x 250
Resolution (mm)	3x 3 x 3	3 x 3 x 3	3 x 3 x 3	2 x 2 x 2
Avg. Acq. Time (min)	3.05	3.05	3.05	3.05
Cardiac Synchronisation	Retrospective	Retrospective	Retrospective	Retrospective
Cardiac Phases	10	10	10	10
T_{enc} (mm/2π)	1	1	1	1
Decoding Delay	200	-	-	-
Temporal Resolution (ms)	75	140	140	140
Encoding Direction	FH	FH	FH	FH

TE – Time of Echo; TR – Time of Repetition; FOV – Field of View; Avg. Acq. Time – Average Acquisition Time; FH – Feet-Head.

3.2. Image Processing Pipeline

The imaging processing pipeline of this project is herein outlined. Furthermore, this section is divided into three sub-sections, each one dealing with the different steps that takes to convert an MRI raw image into an image that can be analysed. In fact, **Section 3.3.1** addresses the registration processes followed by **Section 3.3.2** that outlines how the segmentation was conducted. Lastly, **Section 3.3.3** describes the eddy current correction method used for the PC-MRI sequence that was used in this project.

3.2.1. Coregistration

In this project, coregistration was obtained using the Statistical Parametric Mapping (SPM12) (Welcome Trust Centre for Neuroimaging, University College London), which is a toolbox available on MATLAB (MathWorks, Natick, MA, USA) software. The decision to use this toolbox resulted from several factors. Firstly, as the different image modalities were acquired in the same session, it was assumed that no structural changes occurred and, therefore, the coregistration could be performed using a rigid body model [38]. As a result, it was suggested not only by the literature but also by the team working on this project to use SPM. Secondly, SPM is a toolbox that has a simple interface and accessibility, which was also taken into consideration.

In SPM, coregistration is achieved using a rigid body model that consists of two steps. The first step consists of estimating parameters that are then stored in a transformation matrix such as the one described in **equation 2.6**. After the first step, the image is then transformed using the transformation matrix in order to best match the reference image. Furthermore, it is necessary to choose an interpolation method to fill in the data spaces.

In this project, the reference image corresponded to the 3D-T1w image. Moreover, both PC-MRI and DENSE images were coregistered, using SPM in order to best match the reference image. Regarding the interpolation method, the one used in this project was the *trilinear interpolation*, a simple interpolation that still has better results than a faster method such as the *nearest neighbor*.

3.2.2. Segmentation

Like the coregistration step in this project, the SPM toolbox was used in order to perform segmentation. However, it was suggested that the Computational Anatomy Toolbox (CAT) (Jena University Hospital, Departments of Psychiatry and Neurology), an SPM toolbox, provided better results. Due to this work's nature, the critical part of this segmentation relied on the segmentation of CSF. As a result, the original CAT script was slightly altered in order to allow this program to save the CSF segmented images directly. This software was used to segment the T_1-weighted images into CSF, GM and WM probability maps. Additionally, voxels in the CSF tissue mask with a probability less than 0.95 were removed from the mask.

3.2.3. Eddy Current Correction

Phase Contrast MRI images need to be corrected for the eddy currents artifacts as this background velocity offset error accumulates and leads to significant errors [43]. Since three velocity encoding directions were acquired, all of these orientations need to be corrected individually. The eddy current correction method used in this project was performed assuming that the background offset changes linearly across the image, more precisely in the axis of the velocity encoding direction it was acquired. Additionally, it was assumed that the background offset was time-constant, meaning that it did not alter from one cardiac phase to another.

To correct this artifact, a MATLAB script was created. The script broadly takes a DICOM MRI image and creates two different masks based on the image magnitude values: the first mask consists of stationary tissue and the second of CSF. To do this, two thresholds were created for each type off tissue.

The stationary, or static tissue, has a much higher intensity threshold when compared to the CSF threshold. Following this step, the velocities of each stationary voxel were extracted as well as its location. Using both the velocity values and the voxels' location, a gradient was created using a polynomial fit of the first order. Finally, this gradient, which represents the background offset, is subtracted from the velocity images, which allows for the eddy current effect to be corrected.

3.3. Regions of Interest Selection

In this project, several anatomical regions were analysed. These regions were selected based on two criteria. The first one consists of choosing regions that correspond to the ventricular space, such as the Lateral Ventricles, the Third and Fourth Ventricle, the Aqueduct of Sylvius, and the Cisterna Magna. Additionally, more broad regions were selected. These regions correspond to larger areas in the periphery of the brain and cannot be entirely defined, *i.g*, superior and inferior brain; posterior and anterior brain.

After that, the ventricular regions were selected by creating anatomical masks on the 3D-T1w image, and then, these masks were used to segment the velocity images. This method was used to select eight different regions (as there are two lateral ventricles) that are highlighted and described in **Figure 3.1**.

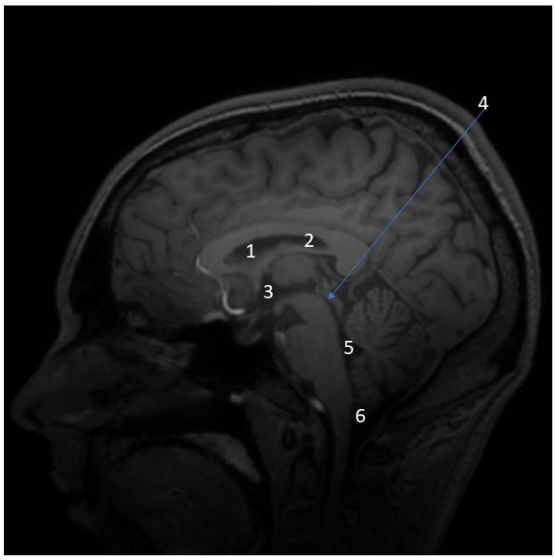

Figure 3.1: MRI T1-w image (Subject 1). The numbers represent different anatomical structures: anterior lateral ventricle (left and right) (1); posterior lateral ventricle (left and right) (2); third ventricle (3); aqueduct of Sylvius (4); fourth ventricle (5); cisterna magna (6).

Additionally, peripheral regions were selected. In fact, in order to select these regions, the segmented anatomical images obtained using CAT were used. More precisely, the CSF tissue images were used in order to create a CSF mask for each volunteer. Then, this CSF mask was used on the velocity images to obtain velocity images exclusively containing CSF. Moreover, these new images

were then divided into six different regions by analysing their anatomy. The regions selected are highlighted and described in **Figure 3.2**.

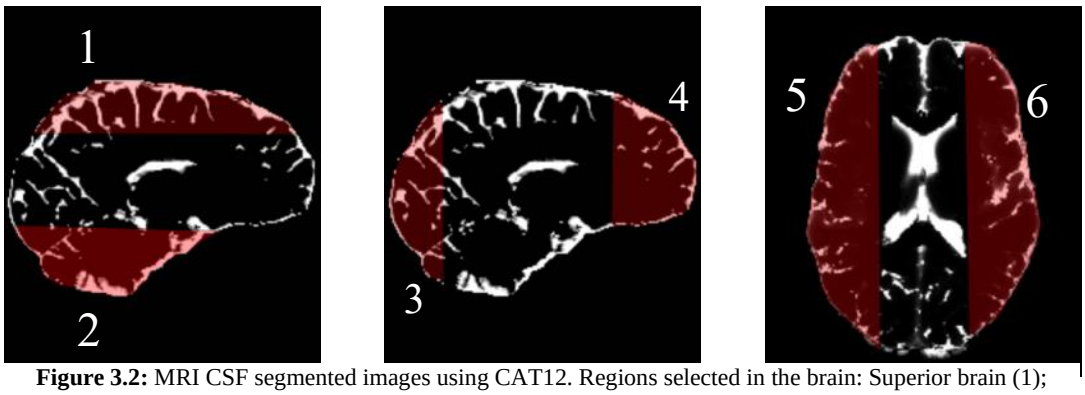

Figure 3.2: MRI CSF segmented images using CAT12. Regions selected in the brain: Superior brain (1); Inferior Brain (2); Posterior Brain (3); Anterior Brain (4); Right Brain (5); Left Brain (6).

3.4. Velocity Analysis

After selecting the regions, the velocity values for each voxel within these ROIs were obtained and the mean velocity of each region was computed. Therefore, for each region, the mean velocity values for each cardiac phase were obtained. By convention and as used in Philips MRI scans, for feet-head acquisitions, positive velocities are in the head direction, negative in the feet direction; for right-left acquisitions, positive velocities are in the left direction, negative in the right direction; and finally, for anterior-posterior acquisitions, positive velocities are in the posterior direction, negative in the anterior direction.

3.5. Displacement Analysis

3.5.1. PC-MRI

Apart from the CSF velocity analysis in this work, the displacement of this fluid was also analysed. As stated previously, PC-MRI is used to obtain velocity maps, not displacement. However, it is possible to mathematically transform the former into the latter. Displacement is the difference between the final and initial position of a point trajectory. Therefore, it can be obtained by integrating the velocity over time, as represented in **Equation 3.1**:

$$\Delta x = \int_{t_i}^{t_f} \boldsymbol{v}(t)\, dt \qquad \text{(Equation 3.1)}$$

The velocity values within the previously selected regions were then integrated in order to obtain displacement values, which were then averaged out. Therefore, it is possible to analyse each voxel's displacement, or region, from one cardiac phase to another.

3.5.2. DENSE

To use the images obtained from the DENSE sequences to make a displacement analysis, it is necessary to compute the original DICOM images and process them so that the displacement maps can be produced. The fundamental aspect of this process consists of the transformation of the phase image into displacement. Since the measured phase is usually wrapped onto the range of [-π, +π], phase unwrapping is required in order to visualize the correct images.

To perform phase unwrapping, over the cardiac cycle, the phase image was multiplied with the chosen T_{enc}, and, consequently, the resultant image is given in *mm*. Residual offsets in the displacement maps were corrected by subtracting the first acquired cardiac phase from the remaining phases.

Furthermore, the displacement images of the entire brain were then segmented into the same regions as the ones presented in **Section 3.3.** However, as displayed in **Table 3.2**, the DENSE images were acquired with a 2 and 3 mm isotropic resolution. This low spatial resolution meant that some regions of the brain that are too small, such as the aqueduct, could not be segmented with a high degree of accuracy and certainty. Despite the fact that larger regions of the ventricular system could still be analysed, such as the lateral ventricles, for consistency reasons only the regions displayed in **Figure 3.2** were taken into consideration for this section of the project**.**

4. Results

Chapter 4 is divided into three subsections. **Section 4.1** shows the results regarding the correction of the eddy current correction. Next, **Section 4.2**, which consists of this project's core results, displays the velocity **(Section 4.2.1)** and displacement **(Section 4.2.2)** values obtained in every region of the brain analysed. Finally, **Section 4.3** shows how different DENSE acquisitions compare to the PC acquisition for one subject.

4.1. Eddy Current Correction

A threshold was used to separate the static from the moving tissue, using the magnitude image and, consequently, creating a static tissue mask. An example of the mask (computed from Subject 1) is presented in **Figure 4.1.**

Figure 4.1: Static tissue mask obtained from the magnitude image of a PC-MRI acquisition (Subject 1).

From this mask, it was possible to calculate a polynomial fit that shows how the velocity of the static tissue changes based on its location. Using this polynomial fit, a gradient was created that represents the effect of the eddy currents on the image. This gradient is displayed on **Figure 4.2.**

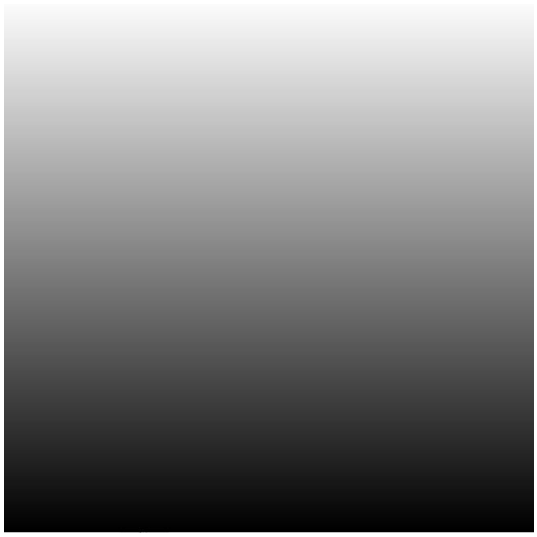

Figure 4.2: Gradient created using the polynomial fit obtained from the static tissue.

Finally, the gradient was subtracted from the velocity image ensuring the correction of the eddy currents was performed. An example of this correction (computed from Subject 1) is presented in **Figure 4.3.**

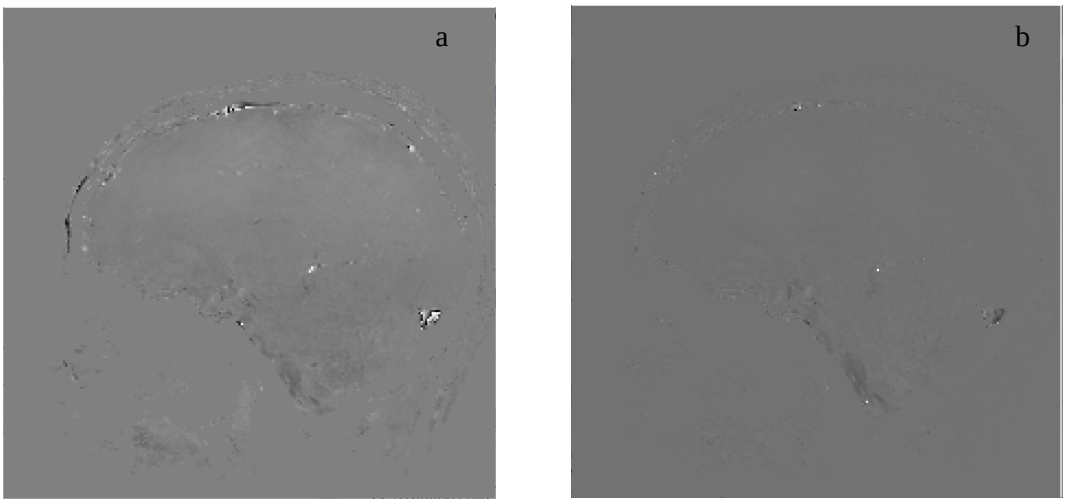

Figure 4.3: Sagittal slice of a velocity image obtained with PC-MRI (Subject 1) before eddy current correction (a); after eddy current correction (b).

Figure 4.3 (a) shows the velocity image obtained using Phase Contrast MRI before the eddy current correction. In this figure, it is possible to see areas that have bright intensity despite the fact of being located in static regions. Therefore, it was necessary to correct the eddy current artifact. By subtracting the gradient displayed in **Figure 4.2** these locations now show darker intensity, which means that the artifact was mitigated **Figure 4.3 (b)**.

4.2. Phase Contrast

4.2.1. Velocity

The velocity results are divided into different regions and presented in a particular order. Firstly, ventricular regions shown in **Figure 3.1** are displayed. Next, the results regarding the peripheral regions are presented. Furthermore, this section focuses on the analysis of four subjects. However, one of these subjects only has data relating to the Feet-Head encoding direction since this encoding direction was the only one acquired (Subject 4). The first region analysed corresponds to the anterior ventricles, both right and left. Furthermore, as the triggering was performed using a peripheral pulse oximeter in two subjects, the cardiac phases were rearranged to resemble the cardiac cycle. Additionally, the last phase corresponds to the first phase as it was added to resemble a full cardiac cycle.

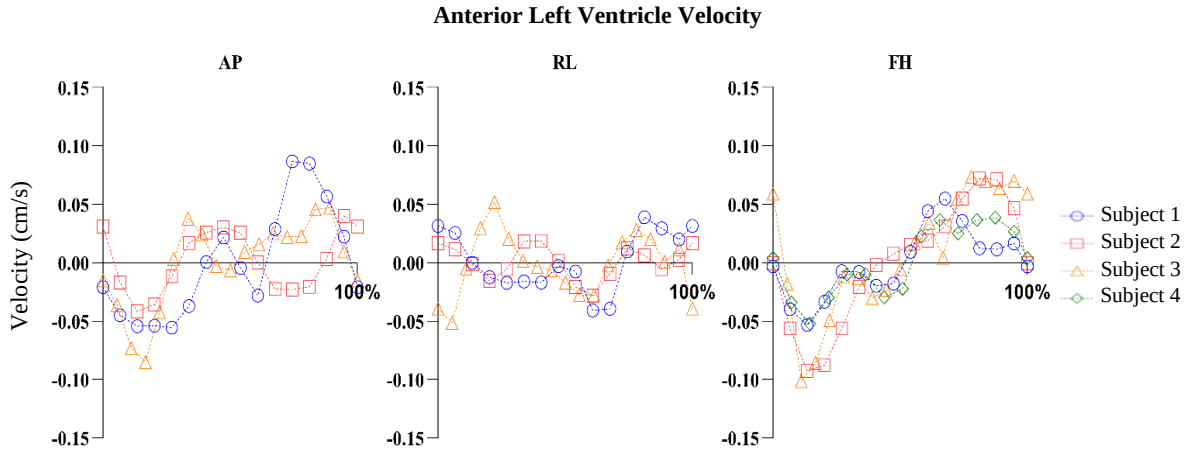

Figure 4.4: Average CSF velocity in the anterior left ventricle, over a full cardiac cycle for three different encoding directions: AP – Anterior-Posterior; RL – Right-Left; FH – Feet-Head.

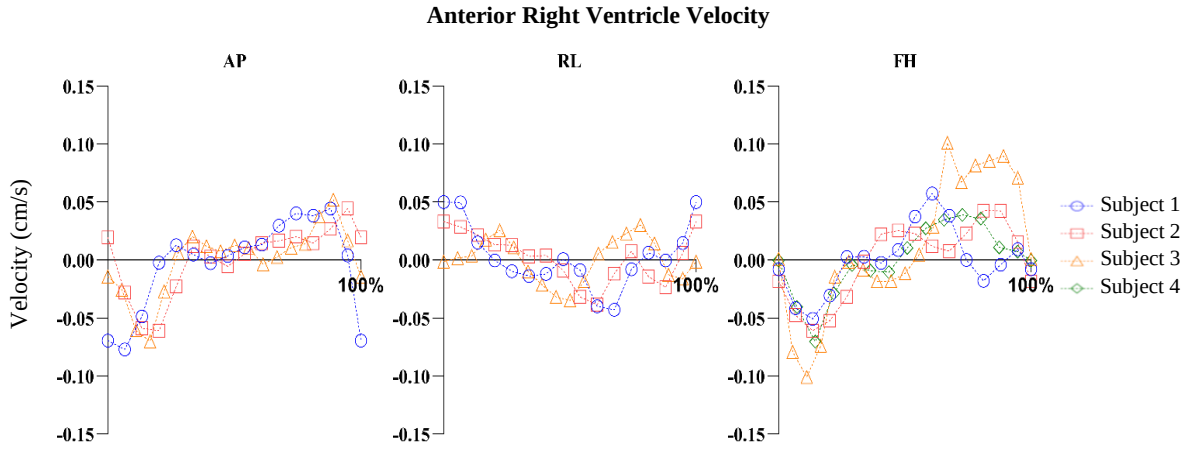

Figure 4.5: Average CSF velocity in the anterior right ventricle, over a full cardiac cycle for three different encoding directions: AP – Anterior-Posterior; RL – Right-Left; FH – Feet-Head.

Figures 4.4 and **4.5** show CSF flow in the anterior left and anterior right ventricles. Following the ventricular system circulation, both left and right posterior ventricles were analysed, and the results are presented in **Figures 4.6** and **4.7**, respectively.

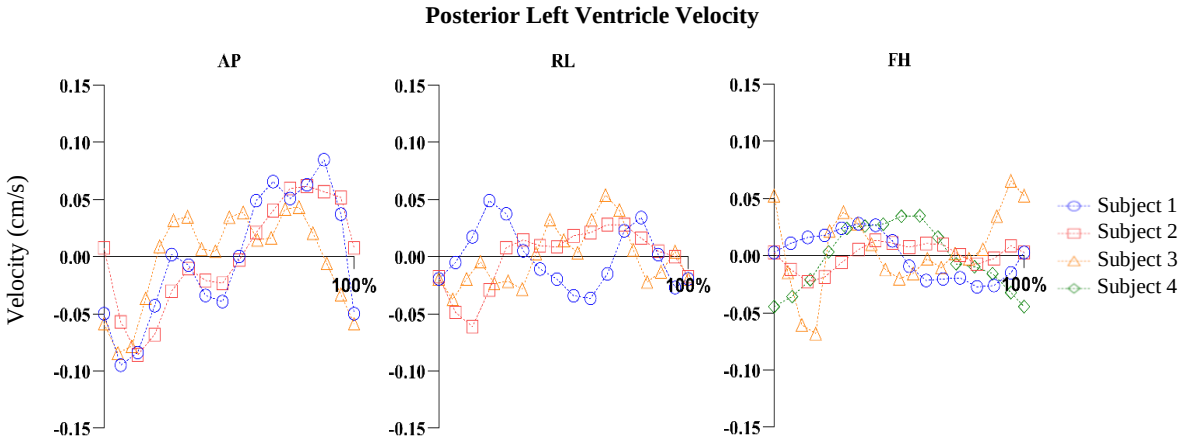

Figure 4.6: Average CSF velocity in the posterior left ventricle, over a full cardiac cycle for three different encoding directions: AP – Anterior-Posterior; RL – Right-Left; FH – Feet-Head.

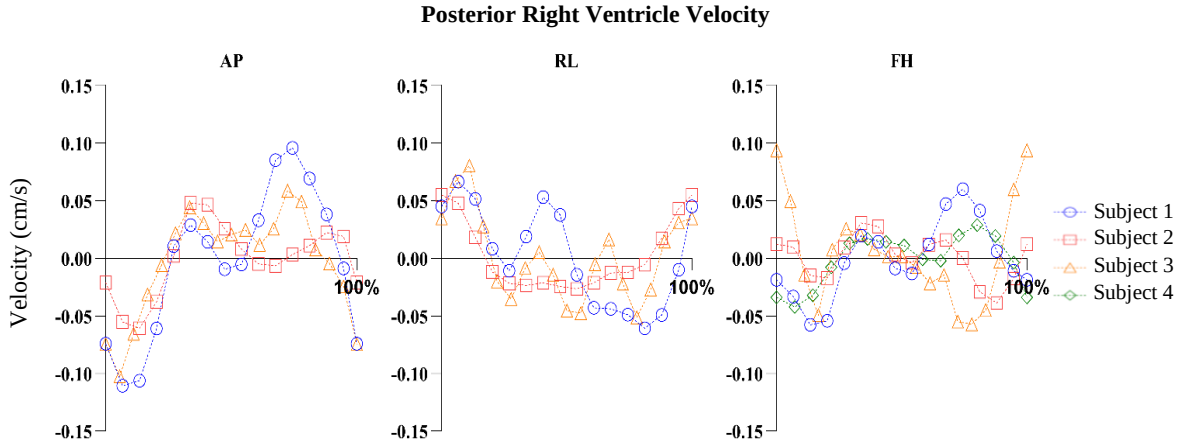

Figure 4.7: Average CSF velocity in the posterior right ventricle, over a full cardiac cycle for three different encoding directions: AP – Anterior-Posterior; RL – Right-Left; FH – Feet-Head.

The lateral ventricles show consistent results between different subjects and within each orientation. The velocity in this region is usually in the anterior and feet direction post-systole and shows opposite lateral velocity for each area, which means that CSF flows inwards in these regions.

After exiting the ventricles, the CSF moves towards the third ventricle and from there to the aqueduct of Sylvius. The evolution of the velocity in these areas are displayed in **Figures 4.8** and **4.9**, respectively.

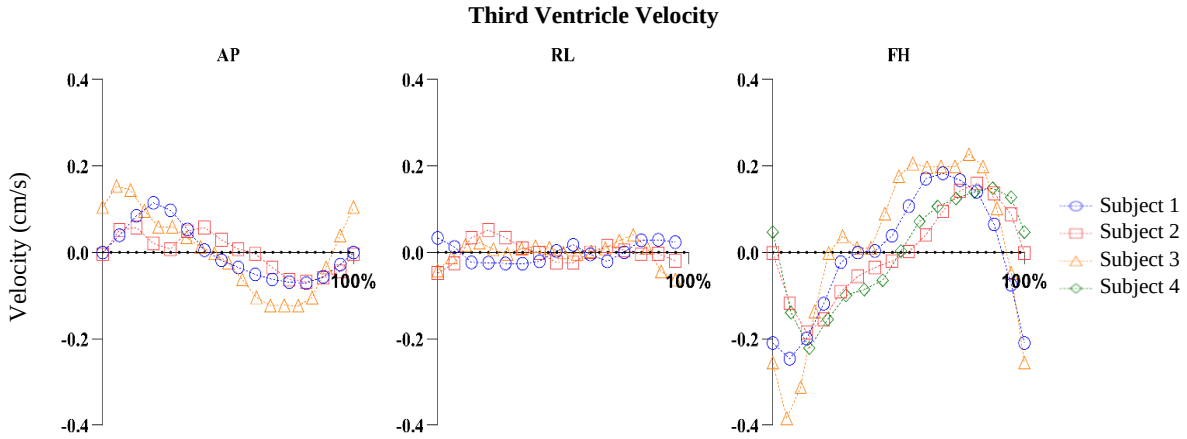

Figure 4.8: Average CSF velocity in the third ventricle, over a full cardiac cycle for three different encoding directions: AP – Anterior-Posterior; RL – Right-Left; FH – Feet-Head.

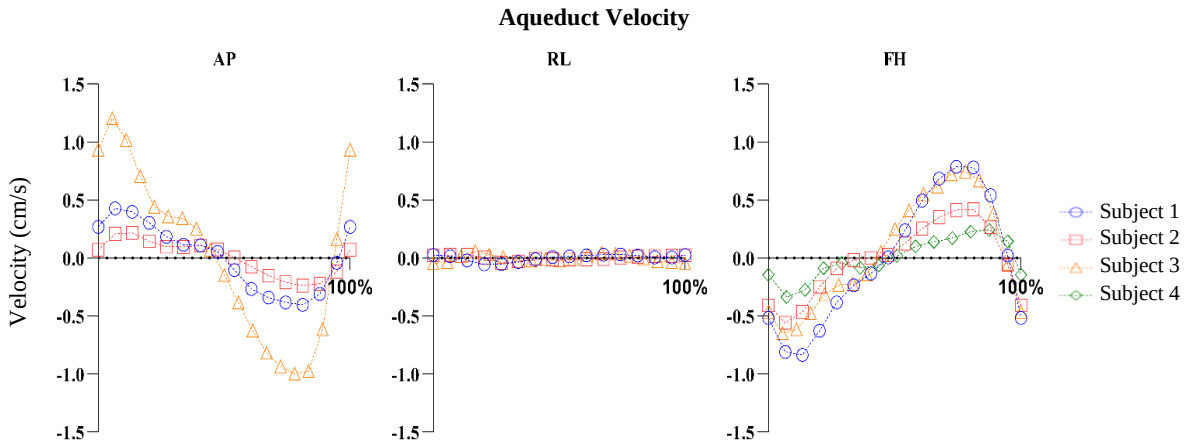

Figure 4.9: Average CSF velocity in the aqueduct, over a full cardiac cycle for three encoding directions: AP – Anterior-Posterior; RL – Right-Left; FH – Feet-Head.

The regions displayed in **Figures 4.8** and **4.9**, that correspond, respectively, to the third ventricle and the aqueduct, show higher values of velocity when compared to the lateral ventricles. Furthermore, both regions show consistent results between subjects, and both show a predominant flow in the posterior and feet direction post systole.

The two final regions of this analysis correspond to the fourth ventricle and the cisterna magna. These are the last cavities in which the CSF travels before leaving the brain and entering the spinal canal. These velocities are represented in **Figures 4.10** and **Figure 4.11.**

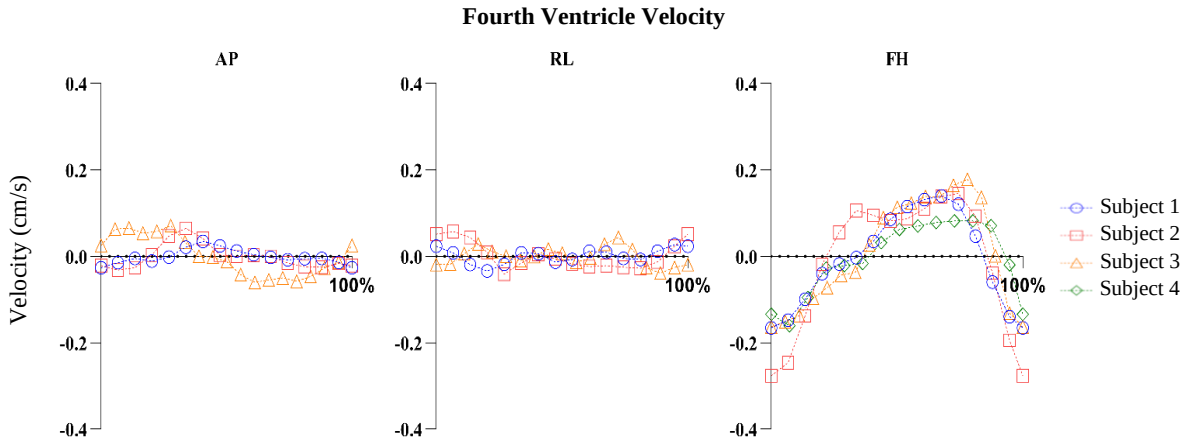

Figure 4.10: Average CSF velocity in fourth ventricle, over a full cardiac cycle for three different encoding directions: AP – Anterior-Posterior; RL – Right-Left; FH – Feet-Head.

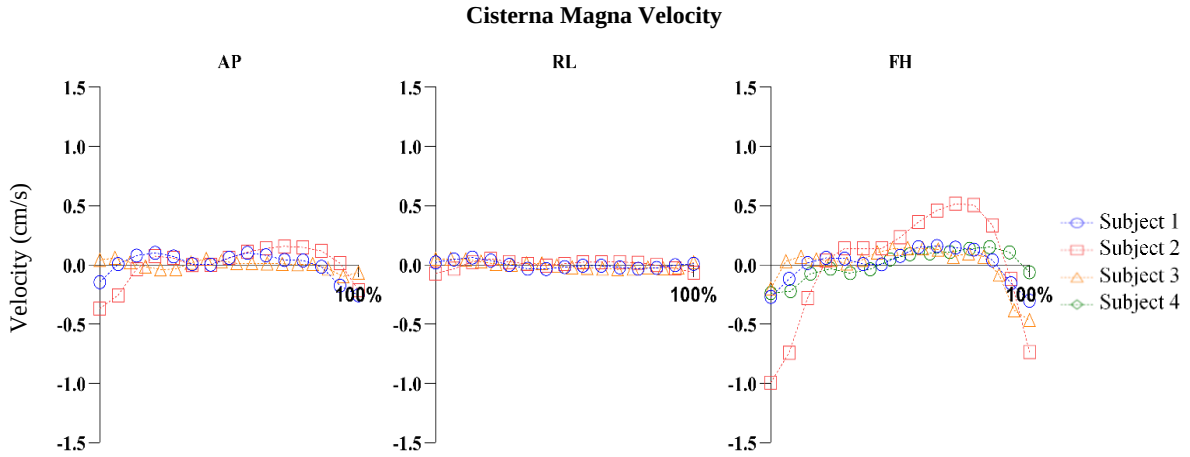

Figure 4.11: Average CSF velocity in the cisterna magna, over a full cardiac cycle for three different encoding directions: AP – Anterior-Posterior; RL – Right-Left; FH – Feet-Head.

By using the velocity values obtained in the ventricular regions, a table containing each region's absolute maximum value and for each encoding direction was computed. Furthermore, the results herein displayed correspond to the maximum across all subjects and the subject that showed the highest value is identified. **Table 4.1** is of particular interest as it allows future sequences to better optimize the parameters for each region, such as the velocity encoding value.

Table 4.1: Maximum absolute velocity in each region in the ventricular system, across all subjects. The number in brackets represents the subject that showed the highest value.

	Maximum Velocity (cm/s)		
Region	AP	RL	FH
Lateral Ventricles	0.09 (1)	0.08 (3)	0.12 (3)
Third Ventricle	0.15 (3)	0.06 (2)	0.38 (3)
Aqueduct	1.20 (3)	0.05 (1)	0.82 (1)
Fourth Ventricle	0.07 (3)	0.06 (2)	0.27 (2)
Cisterna Magna	0.37 (2)	0.07 (1)	0.99 (2)

After analysing the velocity in the ventricular regions, the peripheral regions, presented in **Figure 3.2** were analysed. These regions are analysed pairwise: inferior and superior brain; anterior and posterior brain; and right and left brain. Thus, the first sections of the brain to be analysed correspond to the inferior and superior brain, and their results are presented in **Figure 4.12** and **4.13**, respectively.

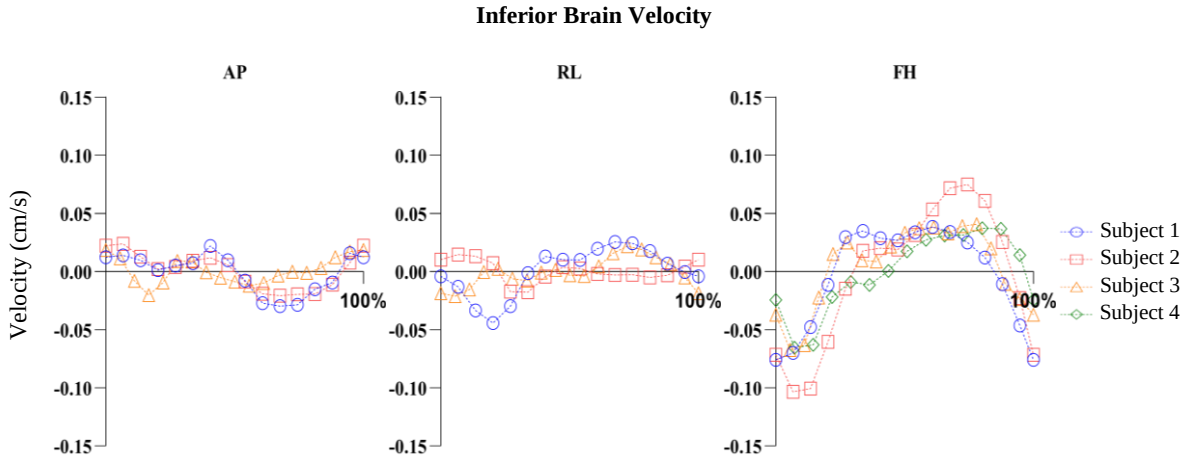

Figure 4.12: Average CSF velocity in the inferior brain, over a full cardiac cycle for three different encoding directions: AP – Anterior-Posterior; RL – Right-Left; FH – Feet-Head.

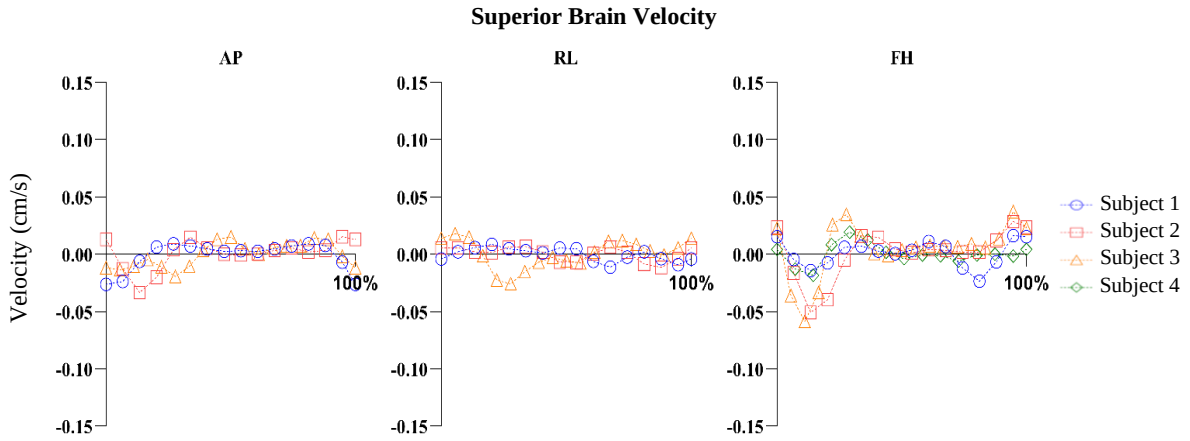

Figure 4.13: Average CSF velocity in the superior brain, over a full cardiac cycle for three different encoding directions: AP – Anterior-Posterior; RL – Right-Left; FH – Feet-Head.

The inferior brain, displayed in **Figure 4.12**, shows the highest velocities when compared to the other brain regions and predominantly in the FH direction.

Figures 4.14 and **4.15** represent the evolution of CSF velocity over the cardiac cycle in the anterior and posterior regions of the brain, respectively.

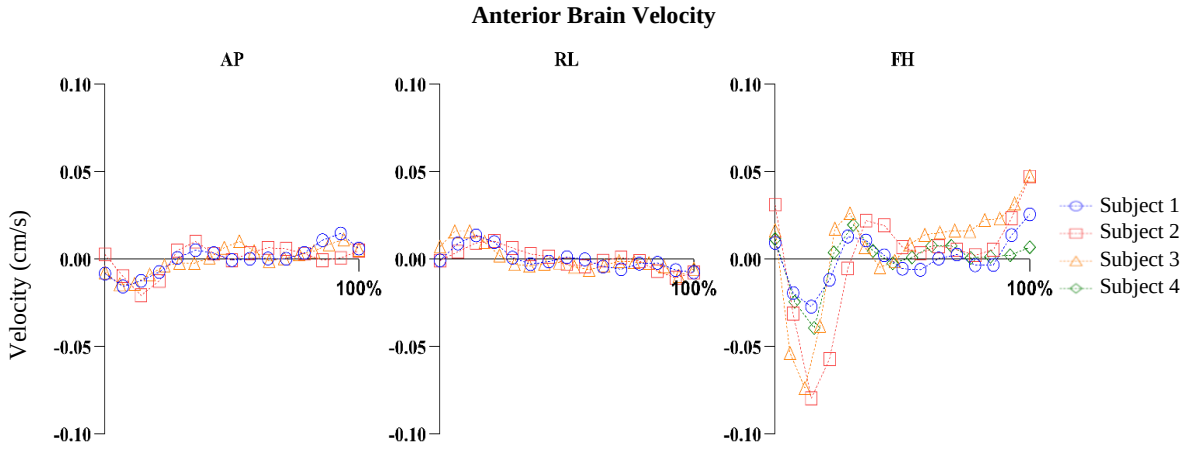

Figure 4.14: Average CSF velocity in the anterior brain, over a full cardiac cycle for three different encoding directions: AP – Anterior-Posterior; RL – Right-Left; FH – Feet-Head.

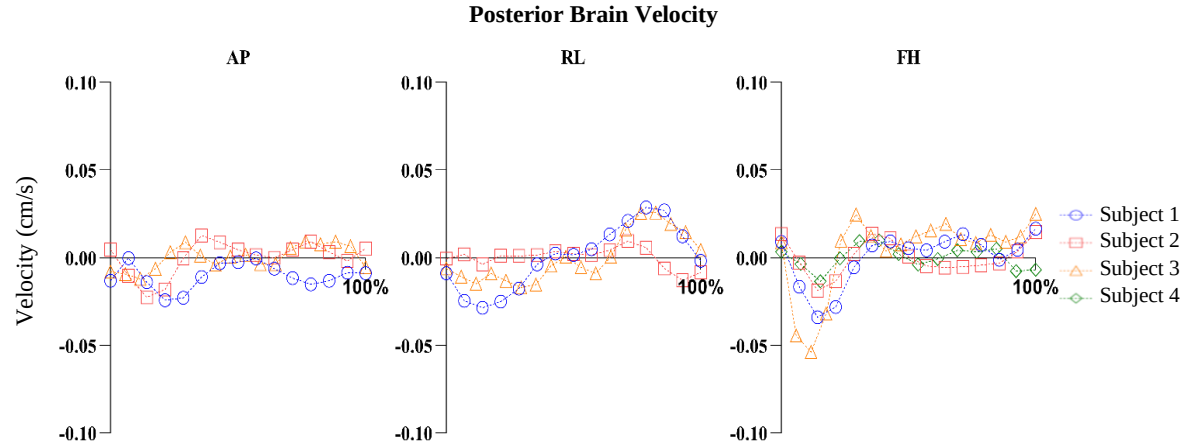

Figure 4.15: Average CSF velocity in the posterior brain, over a full cardiac cycle for three different encoding directions: AP – Anterior-Posterior; RL – Right-Left; FH – Feet-Head.

Lastly, the left and right regions of the brain were analysed. The results corresponding to these particular areas are displayed in **Figure 4.16** and **4.17,** respectively.

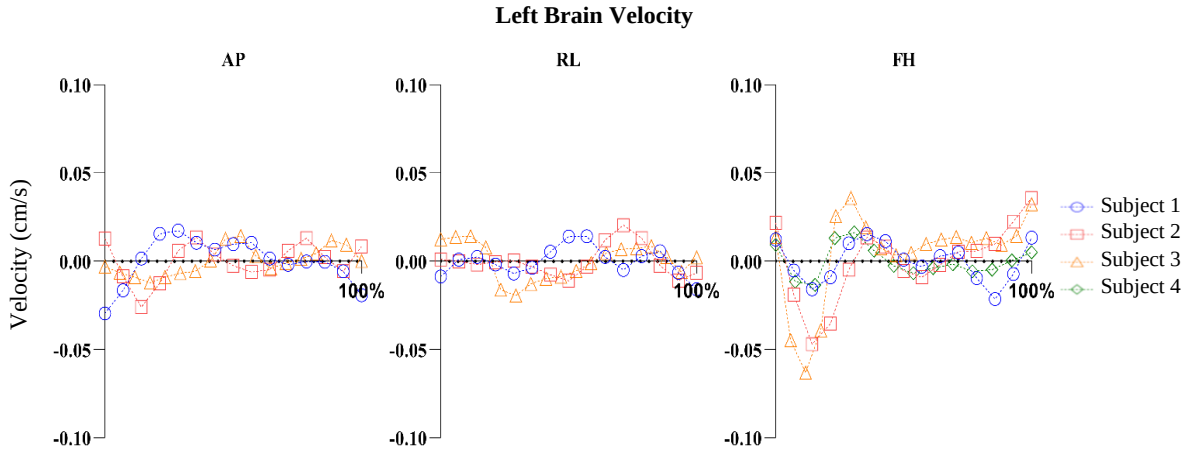

Figure 4.16: Average CSF velocity in the left brain, over a full cardiac cycle for three different encoding directions: AP – Anterior-Posterior; RL – Right-Left; FH – Feet-Head.

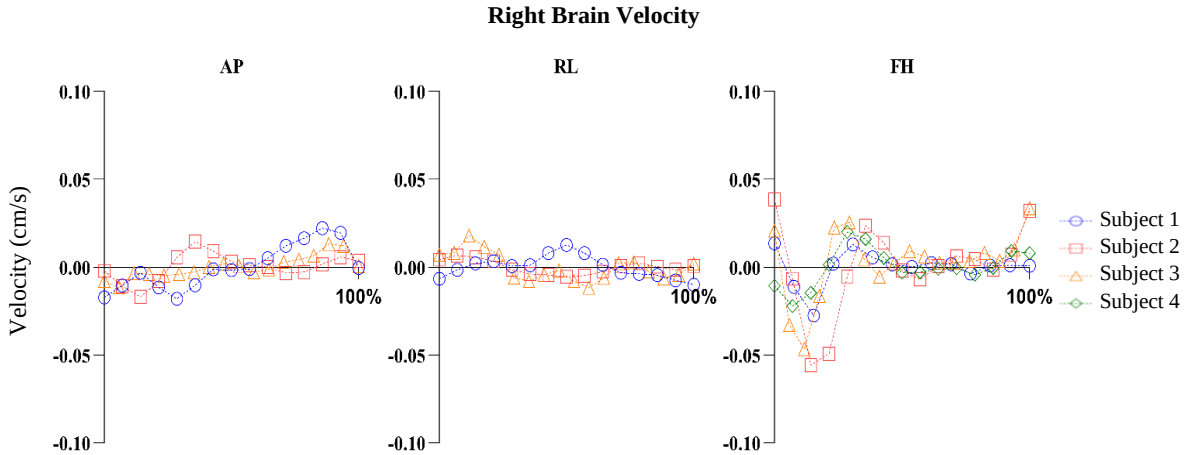

Figure 4.17: Average CSF velocity in the right brain, over a full cardiac cycle for three different encoding directions: AP – Anterior-Posterior; RL – Right-Left; FH – Feet-Head.

In all figures that representing larger brain regions (**Figure 4.12, 4.13, 4,14, 4.15, 4.16,** and **4.17)**, it is possible to see that the highest velocity values occur in the FH encoding direction.

Just like the ventricular regions, **Table 4.2** shows the maximum absolute velocity value for the regions previously analysed.

Table 4.2: Maximum absolute velocity in the larger brain regions, across all subjects. The number in brackets represents the subject that showed the highest value.

	Maximum Velocity (cm/s)		
Region	AP	RL	FH
Inferior	0.02 (1)	0.04 (1)	0.10 (2)
Superior	0.03 (2)	0.03 (3)	0.05 (3)
Anterior	0.02 (2)	0.01 (3)	0.07 (2)
Posterior	0.03 (1)	0.04 (1)	0.06 (3)
Left	0.03 (1)	0.02 (2)	0.07 (3)
Right	0.02 (1)	0.01 (3)	0.06 (2)

4.2.2. Displacement

Using the PC-MRI images, the velocity maps were transformed into displacement maps. The first regions where the displacement was analysed, like the velocity, correspond to the anterior left and right ventricles, and the results are shown in **Figures 4.18** and **4.19.**

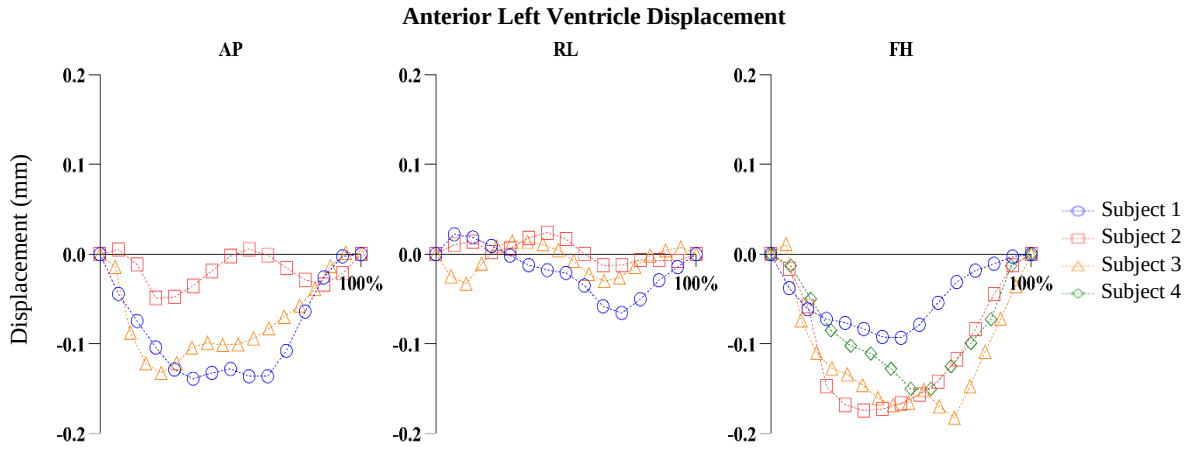

Figure 4.18: Average CSF displacement in the anterior left ventricle, over a full cardiac cycle for three encoding directions: AP – Anterior-Posterior; RL – Right-Left; FH – Feet-Head.

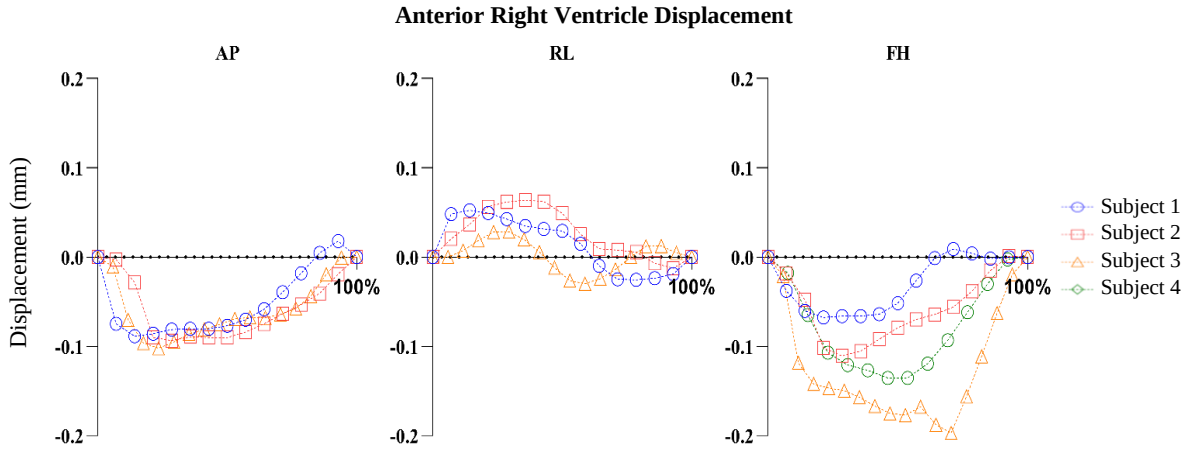

Figure 4.19: Average CSF displacement in the anterior right ventricle, over a full cardiac cycle for three different encoding directions: AP – Anterior-Posterior; RL – Right-Left; FH – Feet-Head.

Subsequently, the displacement was calculated for the posterior left and right ventricles. The results are displayed in **Figure 4.19** and **4.20.**

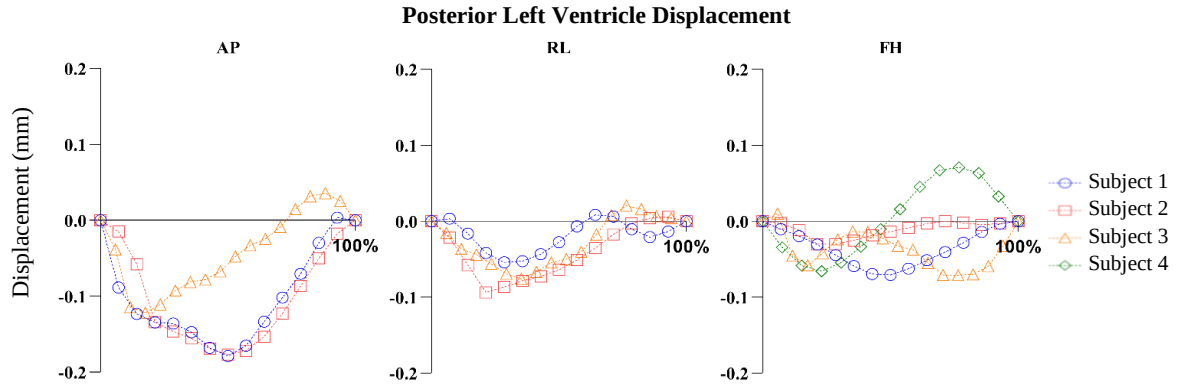

Figure 4.20: Average CSF displacement in the posterior left ventricle, over a full cardiac cycle for three different encoding directions: AP – Anterior-Posterior; RL – Right-Left; FH – Feet-Head.

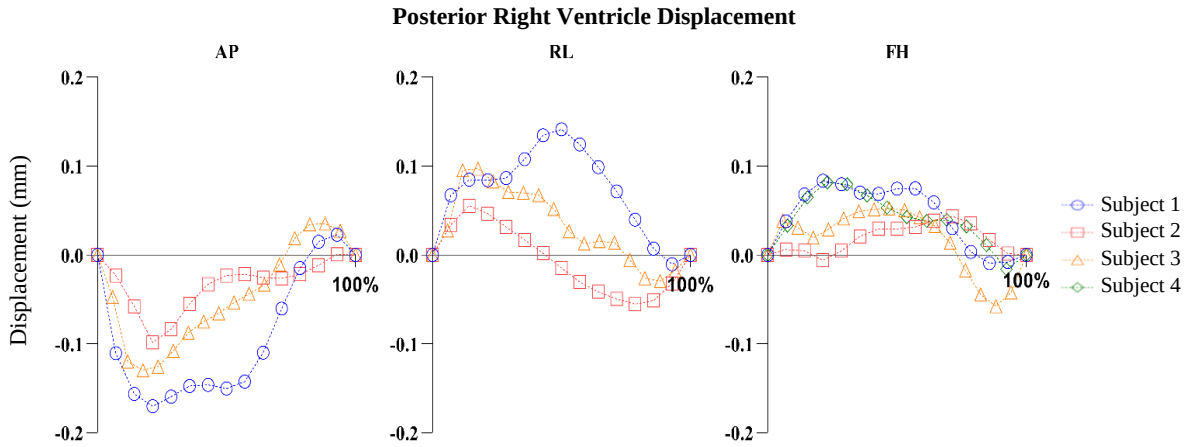

Figure 4.21: Average CSF displacement in the posterior right ventricle, over a full cardiac cycle for three different encoding directions: AP – Anterior-Posterior; RL – Right-Left; FH – Feet-Head.

The lateral ventricles, displayed **in Figures 4.18**, **4.19**, **4.20,** and **4.21**, show that CSF moves, after systole, in the anterior and feet direction. Additionally, the CSF in the lateral ventricles moves inwards as the CSF in the left lateral ventricle moves to the right and the CSF in the right lateral ventricle moves to the left.

After these regions, and following the CSF motion throughout the ventricular system, the displacement for the third ventricular and aqueduct was computed, and it is presented in **Figure 4.22** and **4.23.**

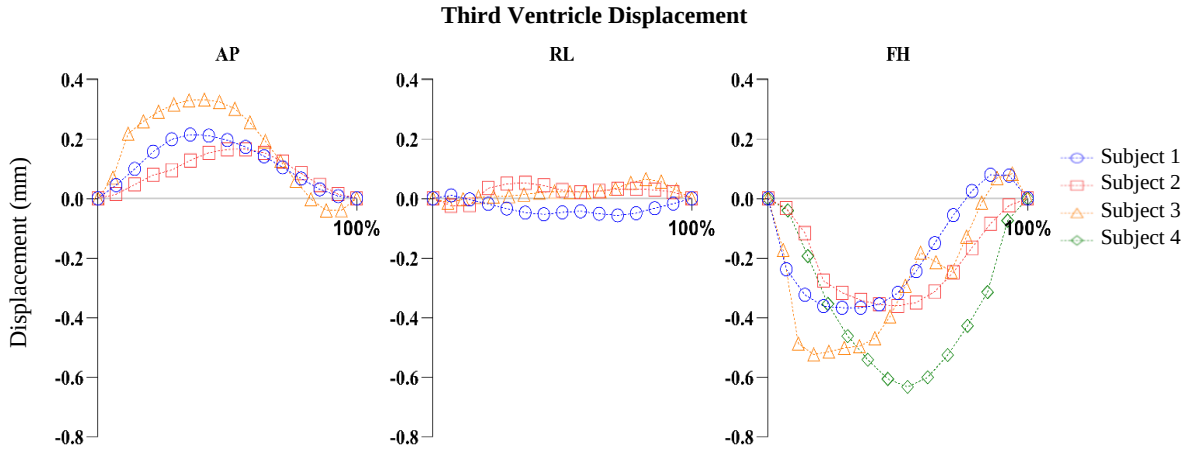

Figure 4.22: Average CSF displacement in the third ventricle, over a full cardiac cycle for three different encoding directions: AP – Anterior-Posterior; RL – Right-Left; FH – Feet-Head.

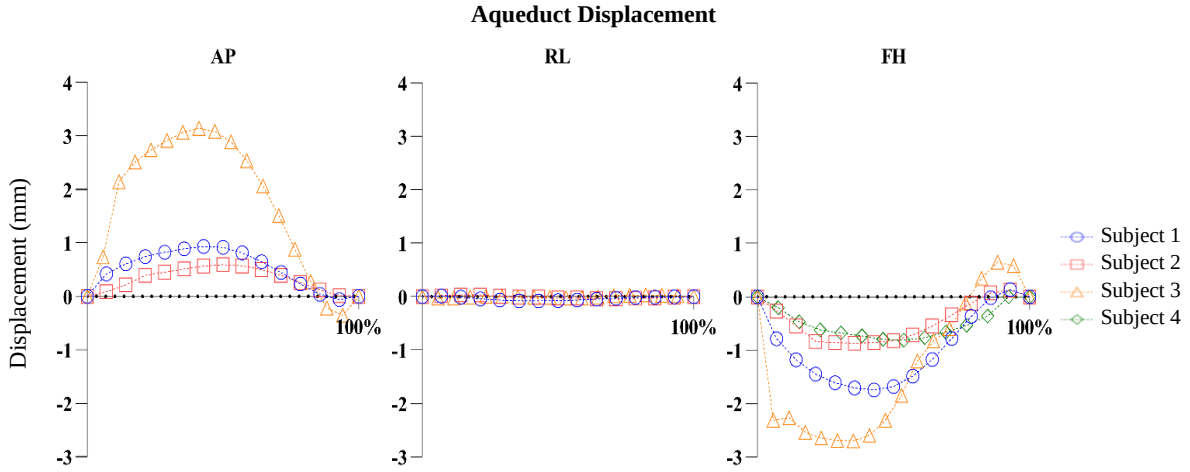

Figure 4.23: Average CSF displacement in the aqueduct, over a full cardiac cycle for three different encoding directions: AP – Anterior-Posterior; RL – Right-Left; FH – Feet-Head.

Next, **Figure 4.22** shows that CSF continues moving in the caudal direction. However, differently from the lateral ventricles, in the third ventricle, CSF flows in the posterior direction, towards the aqueduct. In **Figure 4.23**, which represents the aqueduct, the first aspect worth mentioning is the fact that, for the AP and FH direction, the displacement is ten times larger than for the third ventricle.

Lastly, the results regarding the fourth ventricle and the cisterna magna are shown in **Figure 4.24** and **4.25.**

.

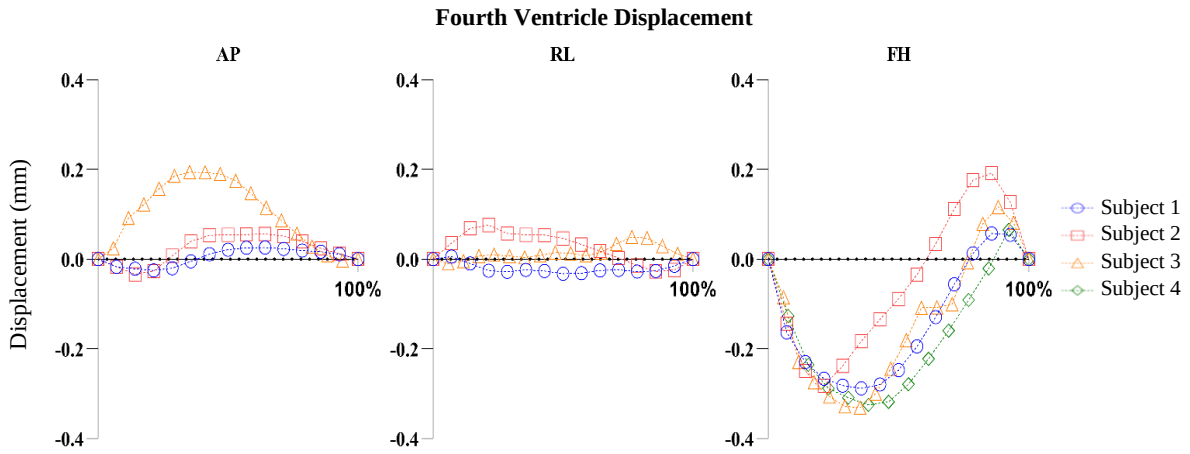

Figure 4.24: Average CSF displacement in the fourth ventricle, over a full cardiac cycle for three different encoding directions: AP – Anterior-Posterior; RL – Right-Left; FH – Feet-Head.

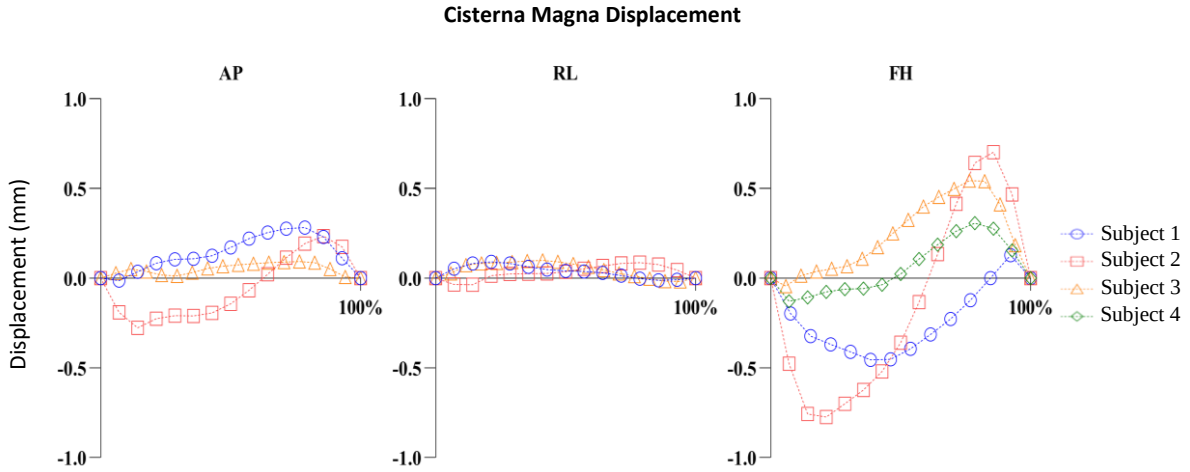

Figure 4.25: Average CSF displacement in the cisterna magna, over a full cardiac cycle for three different encoding directions: AP – Anterior-Posterior; RL – Right-Left; FH – Feet-Head.

Using the displacement values obtained in these regions, the absolute maximum value of each region and for each direction was calculated. Furthermore, the results herein displayed correspond to the maximum between all subjects. These results are displayed in **Table 4.3**.

Table 4.3: Maximum absolute displacement in the ventricular system, across all subjects. The number in brackets represents the subject that showed the highest value.

	Maximum Displacement (mm)		
Region	AP	RL	FH
Lateral Ventricles	0.18 (1)	0.14 (1)	0.19 (3)
Third Ventricle	0.33 (3)	0.01 (1)	0.63 (4)
Aqueduct	3.14 (3)	0.01 (2)	2.70 (3)
Fourth Ventricle	0.19 (3)	0.07 (2)	0.33 (3)
Cisterna Magna	0.28 (2)	0.09 (1)	0.77 (2)

When it comes to displacement values, looking at **Table 4.3,** some conclusions can be drawn from it. Firstly, the most significant displacement values are found in the FH direction and in the AP direction. Furthermore, the RL clearly has smaller displacement values than the two previously mentioned directions. Finally, the aqueduct is the region that displays the highest values of displacement.

After the analysis of the ventricular system, this work focused on the analysis of peripheral brain regions. Like the velocity analysis, the first pair of regions two be analysed corresponds to the inferior and superior part of the brain.

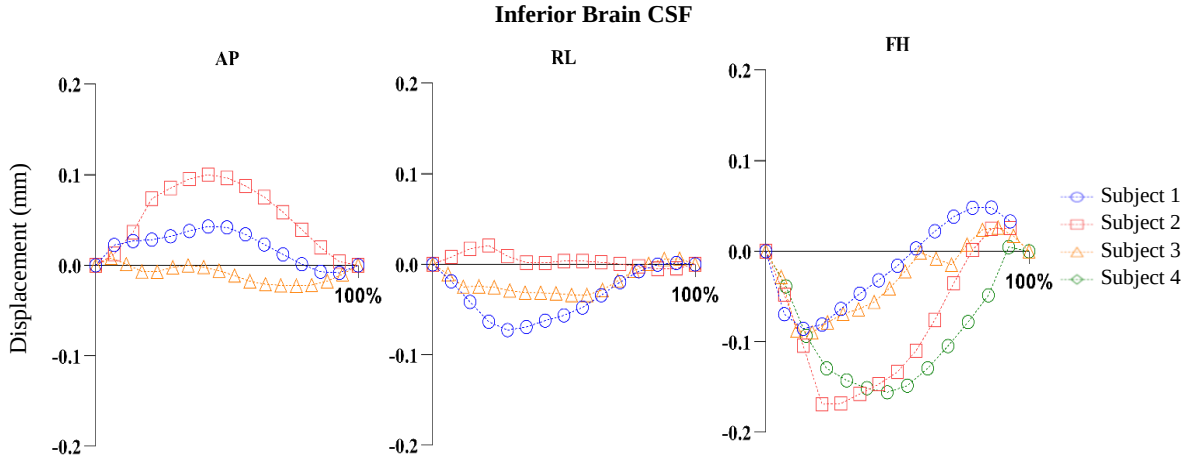

Figure 4.26: Average CSF displacement in the inferior brain, over a full cardiac cycle for three different encoding directions: AP – Anterior-Posterior; RL – Right-Left; FH – Feet-Head.

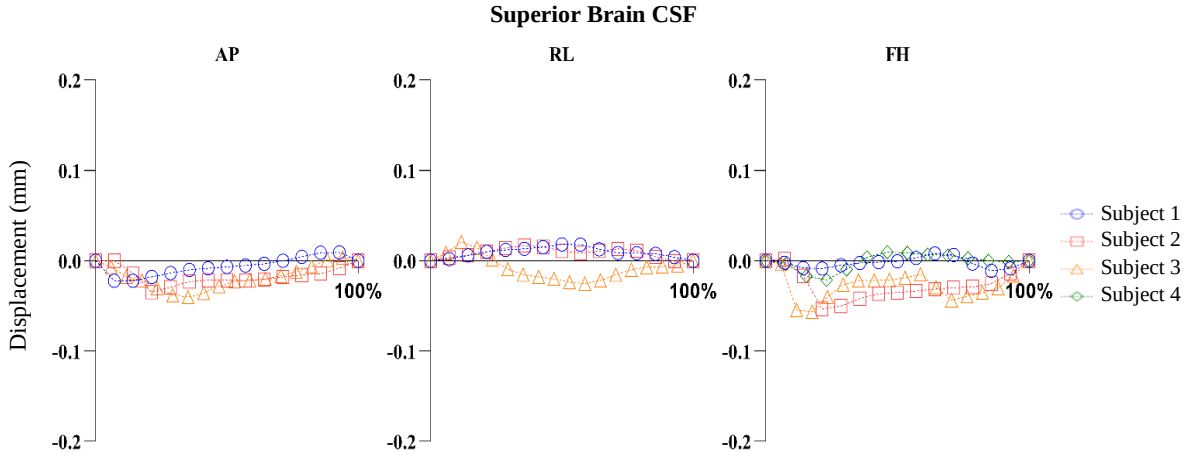

Figure 4.27: Average CSF displacement in the superior brain, over a full cardiac cycle for three different encoding directions: AP – Anterior-Posterior; RL – Right-Left; FH – Feet-Head.

After the inferior and superior brain, the analysis focused on the anterior and posterior regions of the brain, which are displayed in the next two figures.

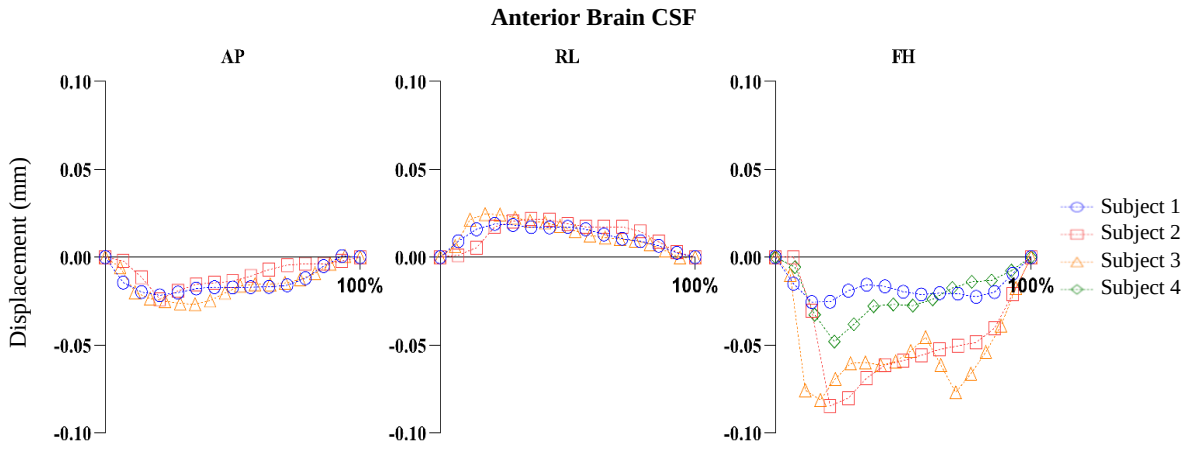

Figure 4.28: Average CSF displacement in the anterior brain, over a full cardiac cycle for three different encoding directions: AP – Anterior-Posterior; RL – Right-Left; FH – Feet-Head.

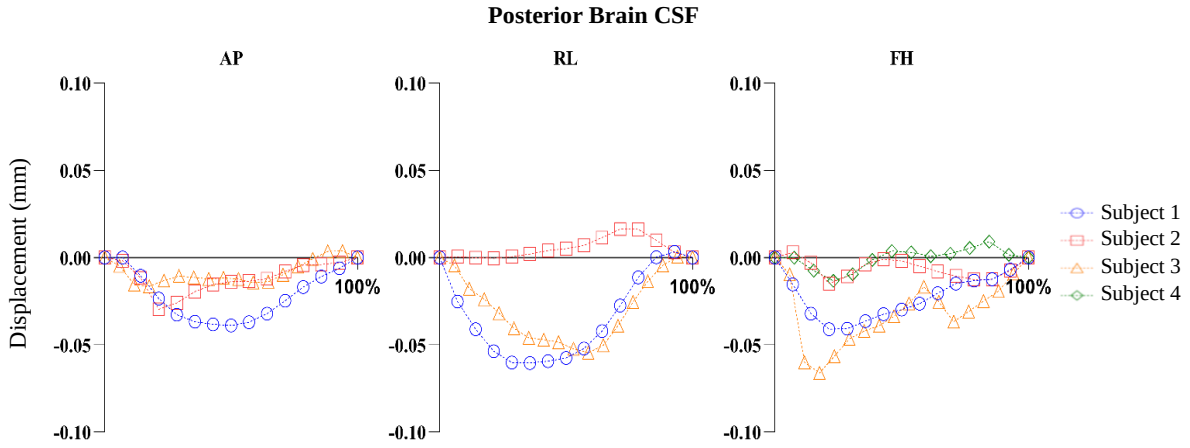

Figure 4.29: Average CSF displacement in the posterior brain, over a full cardiac cycle for three different encoding directions: AP – Anterior-Posterior; RL – Right-Left; FH – Feet-Head

As for the anterior and posterior brain regions, represented in **Figure 4.28** and **4.29**, the CSF in these regions moves in the anterior direction in both regions. Additionally, while in the anterior region CSF moves towards the left direction, in the posterior region CSF moves in the right direction.

Finally, the two last regions to be analysed in the displacement study correspond to the left and right regions of the brain, and the results are shown in **Figures 4.30** and **4.31**:

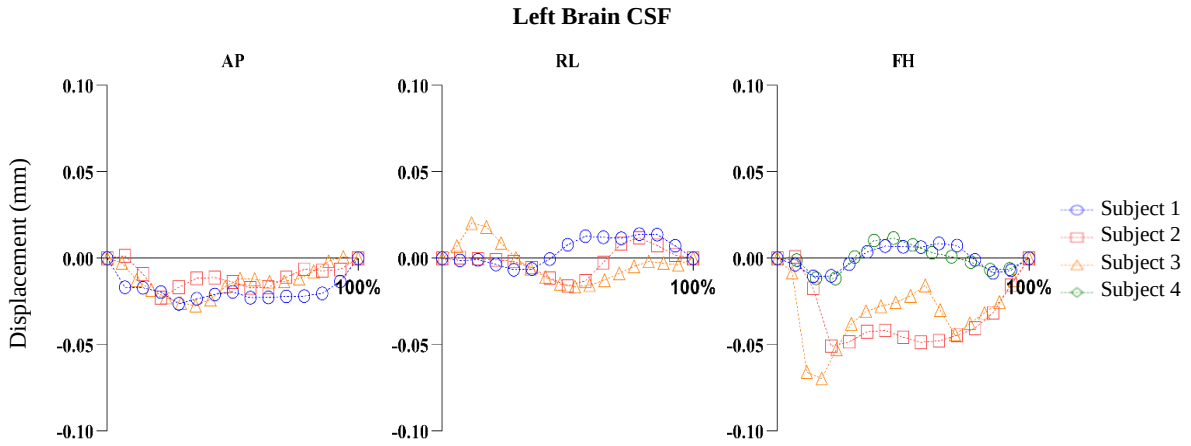

Figure 4.30: Average CSF displacement in the left brain, over a full cardiac cycle for three different encoding directions: AP – Anterior-Posterior; RL – Right-Left; FH – Feet-Head.

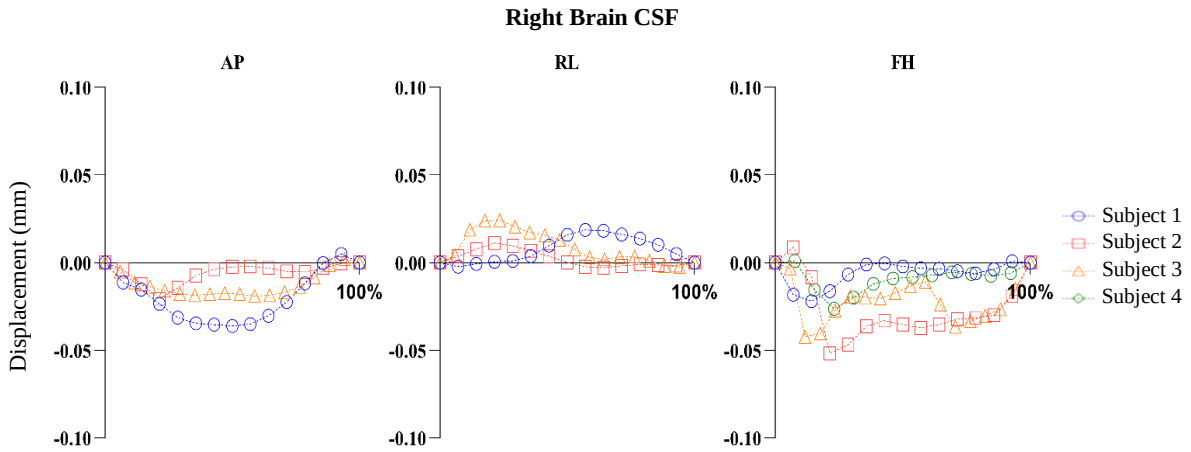

Figure 4.31: Average CSF displacement in the right brain, over a full cardiac cycle for three different encoding directions: AP – Anterior-Posterior; RL – Right-Left; FH – Feet-Head.

The last pair of regions observed were the left and right brain. Both regions show consistent displacement for the AP and FH direction.

Similar to **Table 4.3**, the maximum absolute displacement for each orientation across all subjects was gathered and is displayed in **Table 4.4.**

Table 4.4: Maximum absolute displacement in the larger brain regions, across all subjects. The number in brackets represents the subject that showed the highest value.

	Maximum Displacement (mm)		
Region	AP	RL	FH
Inferior	0.12 (2)	0.07 (1)	0.17 (2)
Superior	0.04 (3)	0.03 (3)	0.06 (3)
Anterior	0.03 (3)	0.02 (3)	0.08 (2)
Posterior	0.04 (1)	0.06 (1)	0.06 (3)
Left	0.02 (3)	0.02 (3)	0.07 (3)
Right	0.04 (1)	0.02 (3)	0.05 (2)

Just like for the ventricular regions, **Table 4.4** shows that the largest displacement values are found in the FH direction. Furthermore, the RL clearly has smaller displacement values than the two previously mentioned directions. Finally, CSF in the inferior region of the brain displays the highest values of displacement.

4.3. DENSE

Using the MRI images obtained from the DENSE sequences, the displacement maps were calculated. The results are presented in this section, and the regions are analysed pairwise, just like in the previous section. As stated in **Section 3.1.2**, the acquisition was only performed in the FH encoding direction. Additionally, the phase contrast velocity-based results are also presented as a frame of reference.

The first regions where CSF displacement was analysed, correspond to the inferior and superior brain, and the results are shown in **Figures 4.32** and **4.33.**

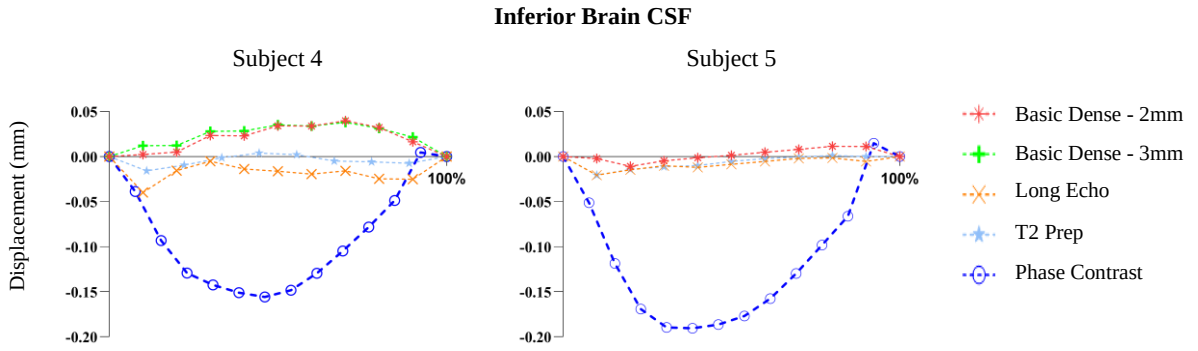

Figure 4.32: Average CSF displacement in the inferior brain over a full cardiac cycle, acquired for the FH direction, for five different acquisition methods.

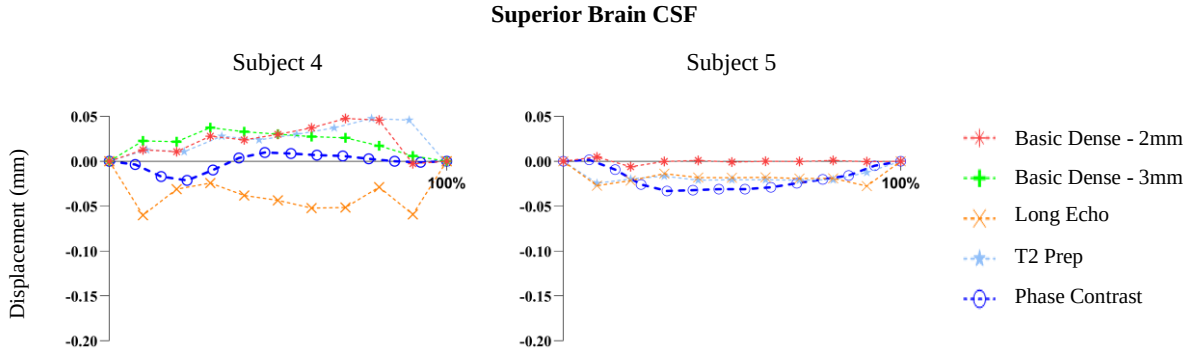

Figure 4.33: Average CSF displacement in the superior brain over a full cardiac cycle, acquired for the FH direction, for five different acquisition methods.

The second pair of regions analysed in this study were the anterior and posterior part of the brain and the corresponding results are displayed in **Figures 4.34** and **4.35:**

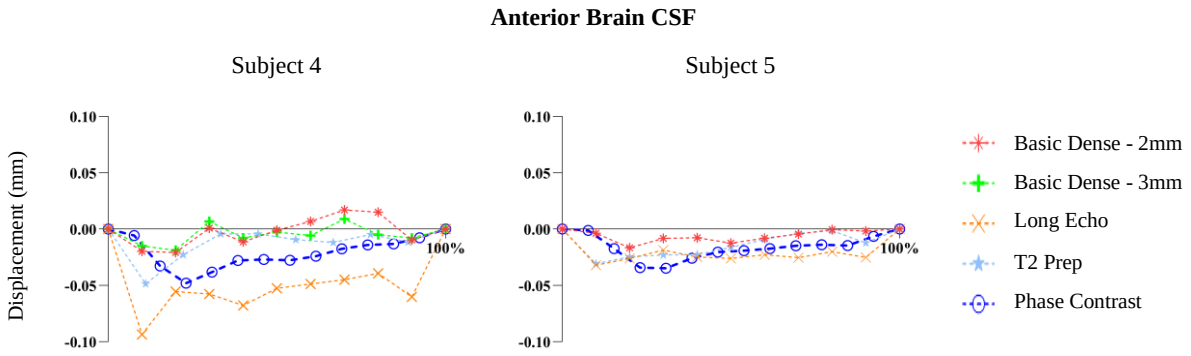

Figure 4.34: Average CSF displacement in the anterior brain over a full cardiac cycle, acquired for the FH direction, for five different acquisition methods.

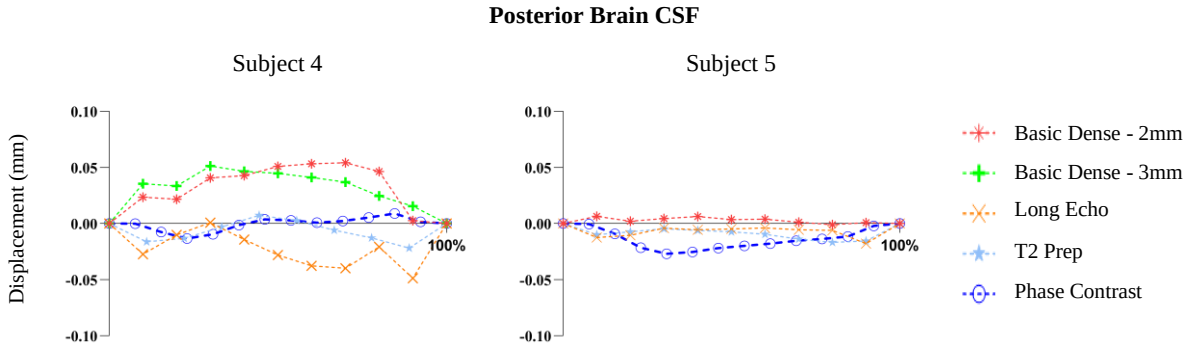

Figure 4.35: Average CSF displacement in the posterior brain over a full cardiac cycle, acquired for the FH direction, for five different acquisition methods.

Finally, the left and right brain regions were analysed, and the results are shown in **Figures 4.36** and **4.37.**

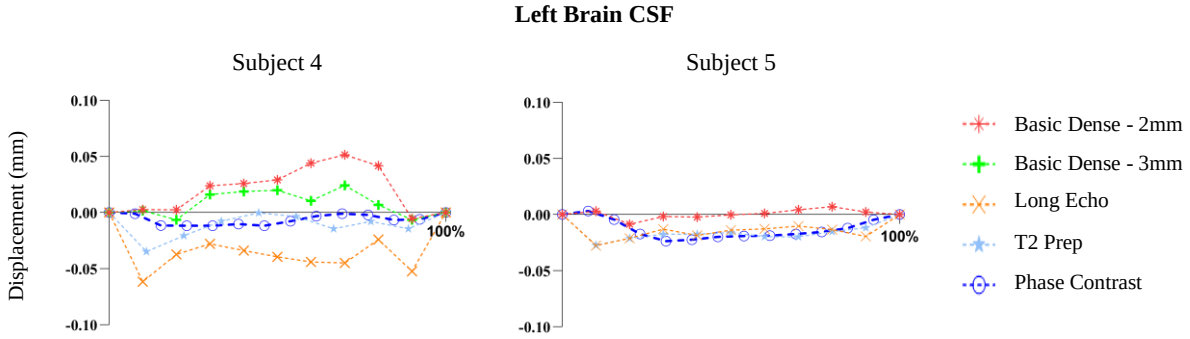

Figure 4.36: Average CSF displacement in the left brain over a full cardiac cycle, acquired for the FH direction, for five different acquisition methods.

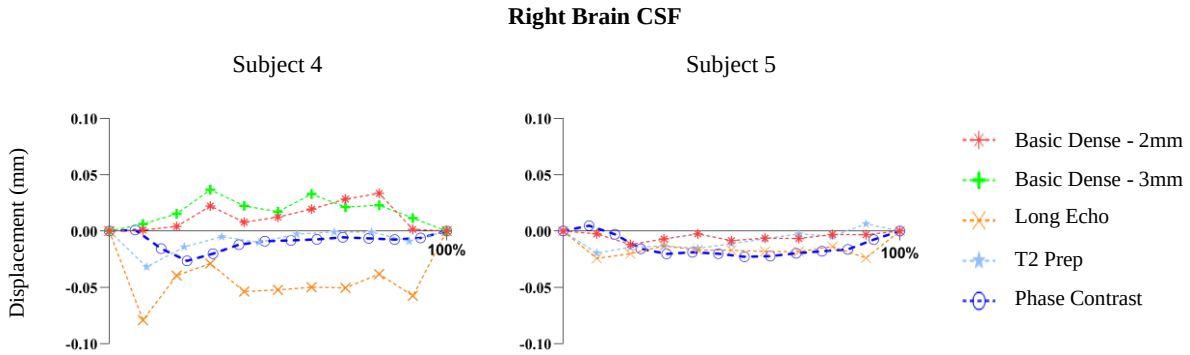

Figure 4.37: Average CSF displacement in the right brain over a full cardiac cycle, acquired for the FH direction, for five different acquisition methods.

5. Discussion

Chapter 5 consists of the discussion of the results obtained and presented in **Chapter 4**. Therefore, in **Section 5.1,** the results regarding the velocity and displacement values are discussed Finally, **Section 5.2** consists of a discussion regarding the displacement values obtained using the different DENSE sequence and the comparison between these and the Phase-Contrast acquisition.

5.1. Phase Contrast

In the first section of this discussion, the results regarding the velocity and displacement analysis obtained with Ultra High Field Phase Contrast MRI, displayed in **Section 4.2.1** and **Section 4.2.2**, are discussed. The acquisitions performed in this dissertation were acquired with retrospective cardiac gating. This method was used since it allows for a more robust correction of eddy currents. In fact, acquiring the cardiac cycle continuously, it is possible to assume that the contribution of a residual gradient caused by this artifact is not time-dependent and, therefore, the contribution to each phase image is constant and can be mitigated by subtracting the gradient to all phase images [73]. Additionally, this method is also less sensitive to irregular heart rates [75].

Using UHF MRI in this project allowed acquiring the Phase Contrast images with high spatial resolution ($1\ x\ 1\ x\ 1\ mm^3$) which reduces the partial volume effect. This is especially important to avoid voxels containing information regarding moving and stationary tissue, which would lead to CSF overestimation.

The analysis of the results regarding both the ventricular regions and the peripheral regions showed consistent results between the four different subjects and within each encoding direction. Nonetheless, differences were identified regarding the encoding direction. The highest velocities, and therefore displacements, were found in the FH direction, which agrees with previous studies that analysed CSF displacement in the brain [80].

Through the analysis of both the velocity and displacement evolution of CSF in the ventricular regions, we can infer this fluid's circulation. The results presented in this study are in agreement with the existing literature regarding CSF circulation [87]. In fact, this work shows that CSF has slow velocities in the lateral ventricles when compared to other ventricular regions [88]. The predominance of CSF displacement in the anterior and in the caudal direction during systole from the lateral ventricles confirms the notion that CSF travels from these regions into the third ventricle [22]. From there, this fluid enters the aqueduct of Sylvius and exits to the fourth ventricle. Furthermore, it is also confirmed that the aqueduct shows the highest velocities in the ventricular region and, consequently, the highest displacement values [89,90]. This acceleration is explained by the continuity equation as the cross-sectional area is much smaller in this region when compared to the third ventricle [88]. For the same reason, the fourth ventricle shows smaller velocity values than the aqueduct and, therefore, acts as a damper.

The mean velocity values obtained in each ventricular region are also in agreement with the majority of reference works that examined the ventricular spaces. The maximum velocity values in the lateral ventricles and in the third ventricle are consistent with the values obtained by Greitz et al. [87]. Additionally, the values obtained in this study for the aqueduct, the most studied region in the ventricular system, agree with the existing literature [87].

The peripheral regions of the brain show slower velocities and displacement values. One factor that might explain these differences in both velocity and displacement is the fact that the bulk of these regions are located in the periphery of the brain. Since CSF motion is caused by the contraction and expansion of the ventricular spaces due to blood entering and leaving the brain [91], it is safe to assume that regions further from the ventricular spaces have slower CSF velocities and, consequently, smaller CSF displacement. Additionally, during the increase in the blood volume caused by the systole, there is mainly inward movement of CSF in the brain, which can be explained by the presence of the skull as it limits this fluid's motion. This occurrence is even more evident when comparing the inferior and superior brain as velocities in the inferior brain are significantly superior to the velocities in the superior brain, which can be explained by the proximity of the former to the heart and to the spinal canal.

Through the analysis of **Table 4.1** and **4.2**, it is evident that the highest values of velocity and displacement for each region and direction are not dominated by a single volunteer. Additionally, the velocities values shown in this project are, for most of the regions selected, much lower than the velocity encoding. Thus, this means that the velocity encoding value chosen was not optimal for these regions and lead to low signal acquisition and lower SNR. The differences found in the velocities for each encoding direction also suggest that the chosen V_{enc} was more suited to a feet-head analysis. However, since the maximum absolute velocities are far below the velocity encoding (5cm/s) we can conclude that if there were aliasing artifacts created by phase wraps present in this study, then its contribution was minimal.

The velocity encoding value chosen can be described as more appropriate for smaller and more central regions, where CSF travels faster, like the aqueduct or the third and fourth ventricle. By contrast, the peripheral regions, such as the inferior and superior brain, show mean velocities almost one hundred times smaller when compared to the velocity encoding. Nevertheless, the consistency of the results supports PC-MRI as a reliable method for CSF velocity assessment, even in regions with lower velocities.

The analysis of the displacement results shows, consistently, that the most significant change in CSF position occurs at the beginning of the cardiac cycle, *i.e.*, during systole. In fact, this corroborates the established theory that CSF motion is driven by vascular pulsatility [19]. The rise of intravascular blood during systole leads to CSF being pushed out of the ventricular spaces as there is a fixed intracranial volume. As the Monroe-Kellie doctrine suggests, the rise of blood volume causes the CSF to be pushed out of the brain into the spinal canal [23]. As the blood leaves the brain during diastole, the vessels relax, and CSF returns to its original position.

Just like the velocity analysis, the displacement analysis shows that the displacement in the periphery is much smaller when compared to the ventricular regions. The wide range of values of displacement found throughout this study poses a challenge when it comes to choosing the best displacement sensitivity. Furthermore, as stated before, the V_{enc} chosen in this project to study the velocity across the brain needs to be optimized depending on the region of interest. It is essential to conduct a more robust study on the periphery of the brain that employs smaller V_{enc} values suitable for these regions, such as 1cm/s, and, consequently, get a better sense of the displacement in these areas.

Recently, several studies [92] have tried to address the complications that arise from using only one velocity encoding value that limits the scope of the study by creating regions where the SNR is lower, due to overestimating this parameter. Alternatives to the single velocity encoding value have been proposed and consist of applying multiple velocity encoding values (Multi-VENC). This method acquires phase information using the different V_{enc} values. However, instead of unwrapping the aliased phase information, this method utilizes the information without phase aliasing acquired by a smaller

V_{enc} to complement this information and, therefore, creating an overlapped velocity field [93,94]. This method showed a two-fold to six-fold increase in the SNR in regions with small velocities. However, applying different velocity encoding values has resulted in longer scan acquisitions, which sometimes comes at the cost of spatio-temporal resolution [95]. Nevertheless, recent studies have tried to solve this issue by combining this method with k-t PCA and Multi-VENC [95] or by using simultaneous multi-Venc and simultaneous multi-slice [96].

5.2. DENSE

In **Section 4.3**, the results regarding the DENSE acquisitions are displayed. Unlike the previous section of this work, where the ventricular regions were also analysed, this part of the project focused on the peripheral regions of the brain, described in **Figure 3.2**. This decision is explained by the low resolution in which these images were acquired. As a result, the region selection and segmentation of the ventricular regions, which sometimes are extremely small, *e.g.*, the aqueduct, could not be performed with a reasonable level of accuracy. Furthermore, the second subject displayed in the results does not show the acquisition for the Basic Dense sequence with 2mm isotropic resolution as the data for this acquisition was lost.

The displacement values obtained using the DENSE sequences were smaller than the displacement sensitivity used in the acquisitions (1mm/2π). The sensitivity employed in this part of the project was much higher than the displacement values obtained, which might have contributed to small phase accumulation [84]. Therefore, this resulted in a smaller SNR. In fact, in regions such as the inferior brain (**Figure 4.32**), there is a significant difference between the PC acquisition and all DENSE methods, which can be attributed to the poor choice of the displacement sensitivity. However, just like the PC-MRI, it is safe to assume that no aliasing effects occurred.

The basic DENSE sequences, with 2 and 3 mm isotropic resolution, show poor consistency with the phase contrast acquisition when compared to the other two DENSE sequences applied. This difference can be attributed to the fact that by using a lower resolution (when compared to the Phase Contrast MRI), the partial effect was more present in the images acquired. Nevertheless, the DENSE sequence that shows more consistency with the Phase Contrast MRI for both subjects is the sequence in which the T_2 preparation was applied. This consistency is especially evident in regions such as the anterior brain (**Figure 4.34)** and the right brain (**Figure 4.37)**. The fact that this sequence shows more consistency with the Phase Contrast acquisition can be explained due to the fact that the T_2 magnetization preparation leads to the mitigation of the partial volume effect.

Some limitations of this dissertation should be addressed. Firstly, the limited number of subjects analysed prevents the results to be statistically analysed and, therefore, to draw more robust conclusions. This is particularly evident in the second part of this project. in which the subjects were analysed using DENSE. Additionally, the lack of clinical patients that present CSF flowing conditions, such as hydrocephalus, prevents this project to show how these conditions reflect on the velocity and displacement of CSF.

6. Conclusion

This work's primary objective was to make a thorough assessment of the velocity of CSF inside the brain and to understand the displacement of this fluid and its relation to the cardiac cycle. An imaging processing pipeline was created so that the 7T MRI data acquired using PC and DENSE protocols could be transformed into velocity and displacement maps. This pipeline consists of several steps, such as coregistration, segmentation, and eddy current corrections.

The velocity and displacement values obtained using PC MRI showed consistent results across subjects for most brain regions. Furthermore, we accomplished the objective of getting a clear picture of the behavior of this fluid in the whole brain and its relation to the cardiac cycle. Additionally, the maximum displacement values obtained for this fluid were used to optimize the DENSE sequences used in the last part of this project. With the exception of the DENSE acquisition that used a T_2 preparation, the DENSE sequences presented in this study showed poor consistency when compared to the Phase Contrast acquisition, which was attributed to the low spatial resolution used in this project and to the fact that the displacement sensitivity was not optimal for analysed regions. Nevertheless, the work carried out in this project lead to the characterization of CSF velocity and displacement across several brain regions, which allows the optimization of future sequences for CSF study.

This work may serve as a starting point for future projects that want to study CSF velocity and displacement in different regions of the brain. Furthermore, future projects in this field can adjust the imaging parameters such as the velocity encoding and the displacement encoding according to the regions of interest. However, it is still necessary to validate the results obtained by analysing more subjects.

One of the most interesting aspects that could follow this project would be to acquire more brain data using DENSE acquisitions with higher spatial resolution, such as 1mm isotropic, which would allow the elimination of the partial volume effect and, therefore, more accurate results and, more importantly, would allow the analysis of displacement in smaller areas. Additionally, the DENSE acquisitions could also be obtained with different encoding orientations, which would allow for a more thorough analysis. Finally, the inclusion of clinical patients would allow understanding how different CSF flowing disorders affect its velocity and displacement.

References

[1] Tom SE, Hubbard RA, Crane PK, et al. Characterization of dementia and Alzheimer's disease in an older population: updated incidence and life expectancy with and without dementia. *Am J Public Health*. 2015;105(2):408-413.

[2] Spector R, Robert Snodgrass S, Johanson CE. A balanced view of the cerebrospinal fluid composition and functions: Focus on adult humans. *Exp Neurol*. 2015; 273:57-68.

[3] Attier-Zmudka J, Sérot JM, Valluy J, et al. Decreased Cerebrospinal Fluid Flow Is Associated With Cognitive Deficit in Elderly Patients. *Front Aging Neurosci*. 2019;11:87.

[4] Cushing H. Studies on the Cerebropinal Fluid: I. Introduction. *J Med Res*. 1914; 31(1):1-19.

[5] Davson H. Formation and drainage of the cerebrospinal fluid. *Sci Basis Med Annu Rev*. 1966; 238-259.

[6] L. Stern & R. Gautier: II. – Les Rapports Entre Le Liquide Céphalo-Rachidien Et Les éléments Nerveux De L'axe Cerebrospinal, Archives Internationales de Physiologie, 1922; 17:4, 391-448.

[7] Abbott NJ. Evidence for bulk flow of brain interstitial fluid: significance for physiology and pathology. *Neurochem Int*. 2004; 45(4):545-552.

[8] Bakker EN, Bacskai BJ, Arbel-Ornath M, et al. Lymphatic Clearance of the Brain: Perivascular, Paravascular and Significance for Neurodegenerative Diseases. *Cell Mol Neurobiol*. 2016; 36(2):181-194.

[9] Betts J Gordon, Young Kelly A, Wise James A. Anatomy and Physiology. Circulation and the Central Nervous System. *Open Stax*. 2016.

[10] Min KJ, Yoon SH, Kang JK. New understanding of the role of cerebrospinal fluid: offsetting of arterial and brain pulsation and self-dissipation of cerebrospinal fluid pulsatile flow energy. *Med Hypotheses*. 2011; 76(6):884-886.

[11] Matsumae M, Sato O, Hirayama A, et al.: Research into the physiology of cerebrospinal fluid reaches a new horizon: intimate exchange between cerebrospinal fluid and interstitial fluid may contribute to maintenance of homeostasis in the central nervous system. *Neurol Med Chir* (Tokyo) 2016; 56: 416–441.

[12] Jessen NA, Munk AS, Lundgaard I, Nedergaard M. The Glymphatic System: A Beginner's Guide. *Neurochem Res*. 2015; 40(12):2583-2599.

[13] May C, Kaye JA, Atack JR, Schapiro MB, Friedland RP, Rapoport SI. Cerebrospinal fluid production is reduced in healthy aging. *Neurology*. 1990; 40(3 Pt 1):500-503.

[14] Silverberg GD, Heit G, Huhn S, et al. The cerebrospinal fluid production rate is reduced in dementia of the Alzheimer's type. *Neurology*. 2001; 57(10):1763-1766.

[15] Stoquart-El Sankari S, Balédent O, Gondry-Jouet C, Makki M, Godefroy O, Meyer ME. Aging effects on cerebral blood and cerebrospinal fluid flows. *J Cereb Blood Flow Metab*. 2007; 27(9):1563-1572.

[16] Feinberg DA, Mark AS. Human brain motion and cerebrospinal fluid circulation demonstrated with MR velocity imaging. *Radiology*. 1987; 163(3):793-799.

[17] Stahlberg F, Mogelvang J, Thomsen C, et al. A method for MR quantification of flow velocities in blood and CSF using interleaved gradient-echo pulse sequences. *Magn Reson Imaging* 1989; 7:655–667.

[18] Maier SE, Hardy CJ, Jolesz FA. Brain and cerebrospinal fluid motion: real-time quantification with M-mode MR imaging. *Radiology*. 1994; 193(2):477-483.

[19] Andreas A. Linninger, Kevin Tangen, Chih-Yang Hsu, David Frim. Cerebrospinal Fluid Mechanics and Its Coupling to Cerebrovascular Dynamics. *Annual Review of Fluid Mechanics* 2016; 48:1, 219-257.

[20] Hladky SB, Barrand MA. Mechanisms of fluid movement into, through and out of the brain: evaluation of the evidence. *Fluids Barriers CNS*. 2014; 11(1):26.

[21] Sloots, J. J., Biessels, G. J. Zwanenburg J. J. M. Cardiac and respiration-induced brain deformations in humans: driving forces of cerebral waste clearance quantified with high-field MRI, *Neuroimage*. 2018; 210.

[22] Enzmann DR, Pelc NJ. Cerebrospinal fluid flow measured by phase-contrast cine MR. *AJNR Am J Neuroradiol*. 1993;14(6):1301-1310.

[23] Greitz D, Wirestam R, Franck A, Nordell B, Thomsen C, Ståhlberg F. Pulsatile brain movement and associated hydrodynamics studied by magnetic resonance phase imaging. The Monro-Kellie doctrine revisited. *Neuroradiology*. 1992; 34(5):370-380.

[24] Bateman GA. Pulse-wave encephalopathy: a comparative study of the hydrodynamics of leukoaraiosis and normal-pressure hydrocephalus. *Neuroradiology*. 2002;44(9):740-748.

[25] Yamada S, Miyazaki M, Yamashita Y, et al. Influence of respiration on cerebrospinal fluid movement using magnetic resonance spin labeling. *Fluids Barriers CNS*. 2013;10(1):36.

[26] Dreha-Kulaczewski S, Joseph AA, Merboldt KD, Ludwig HC, Gärtner J, Frahm J. Identification of the Upward Movement of Human CSF *In Vivo* and its Relation to the Brain Venous System. *J Neurosci*. 2017; 37(9):2395-2402.

[27] Spijkerman JM, Geurts LJ, Siero JCW, Hendrikse J, Luijten PR, Zwanenburg JJM. Phase contrast MRI measurements of net cerebrospinal fluid flow through the cerebral aqueduct are confounded by respiration. *J Magn Reson Imaging*. 2019; 49(2):433-444.

[28] Grover VP, Tognarelli JM, Crossey MM, Cox IJ, Taylor-Robinson SD, McPhail MJ. Magnetic Resonance Imaging: Principles and Techniques: Lessons for Clinicians. *J Clin Exp Hepatol*. 2015;5(3):246-255.

[29] McRobbie DW, Moore EA, Graves MJ, Prince MR. MRI from Picture to Proton. 3rd ed. Cambridge: Cambridge University Press. 2017.

[30] Hendee WR, Ritenour ER. Medical Imaging Physics. 4th ed. New York: Wiley-Liss; 2002.

[31] Chavhan GB, Babyn PS, Thomas B, Shroff MM, Haacke EM. Principles, techniques, and applications of T2*-based MR imaging and its special applications. *Radiographics*. 2009; 29(5):1433-1449.

[32] van Geuns RJ, Wielopolski PA, de Bruin HG, et al. Basic principles of magnetic resonance imaging. *Prog Cardiovasc Dis*. 1999;42(2):149-156.

[33] Duyn JH. The future of ultra-high field MRI and fMRI for study of the human brain. *Neuroimage*. 2012;62(2):1241-1248.

[34] Ladd, M. E., Bachert, P., Meyerspeer, M., Moser, E., Nagel, A. M., Norris, D. G., Zaiss, M. Pros and cons of ultra-high-field MRI/MRS for human application. *Progress in Nuclear Magnetic Resonance Spectroscopy*. 2018; 109, 1-50.

[35] Moser E, Laistler E, Schmitt F, Kontaxis G. Ultra-High Field NMR and MRI–The Role of Magnet Technology to Increase Sensitivity and Specificity. *Front Phys*, 2017; 5:1-15.

[36] Ashburner J, Friston KJ. Unified segmentation. *Neuroimage*. 2005; 26(3):839-851.

[37] Z.Tu, K.L.Narr, P.Dollar, I.Dinov, P.M.Thompson, and A. W. Toga. Brain anatomical structure segmentation by hybrid discriminative/generative models. *IEEE Transactions on Medical Imaging*. 2008; vol.27,no.4,pp.495–508.

[38] A. K. Jain. Fundamentals of Digital Image Processing. Pretince-Hall, 1989.

[39] Despotović I, Goossens B, Philips W. MRI segmentation of the human brain: challenges, methods, and applications. *Comput Math Methods Med*. 2015; 2015:450341.

[40] Lorenz R, Bock J, Snyder J, Korvink JG, Jung BA, Markl M. Influence of eddy current, Maxwell and gradient field corrections on 3D flow visualization of 3D CINE PC-MRI data. *Magn Reson Med*. 2014; 72(1):33-40.

[41] Walker PG, Cranney GB, Scheidegger MB, Waseleski G, Pohost GM, Yoganathan AP. Semiautomated method for noise reduction and background phase error correction in MR phase velocity data. *J Magn Reson Imaging*. 1993; 3(3):521-530.

[42] Lankhaar JW, Hofman MB, Marcus JT, Zwanenburg JJ, Faes TJ, Vonk-Noordegraaf A. Correction of phase offset errors in main pulmonary artery flow quantification. *J Magn Reson Imaging*. 2005; 22(1):73-79.

[43] Gatehouse PD, Rolf MP, Graves MJ, et al. Flow measurement by cardiovascular magnetic resonance: a multi-centre multi-vendor study of background phase offset errors that can compromise the accuracy of derived regurgitant or shunt flow measurements. *J Cardiovasc Magn Reson*. 2010; 12(1):5.

[44] Chernobelsky A, Shubayev O, Comeau CR, Wolff SD. Baseline correction of phase contrast images improves quantification of blood flow in the great vessels. *J Cardiovasc Magn Reson*. 2007; 9(4):681-685.

[45] O'Connel JEA. Vascular factor in the intracranial pressure and maintenance of cerebrospinal fluid circulation. Brain 1943; 66:204-228.

[46] Bering Ea Jr. Choroid plexus and arterial pulsation of cerebrospinal fluid; demonstration of the choroid plexuses as a cerebrospinal fluid pump. *AMA Arch Neurol Psychiatry*. 1955; 73(2):165-172.

[47] Du Boulay GH. Pulsatile movements in the CSF pathways. *Br J Radiol*. 1966; 39(460):255-262.

[48] Enzmann DR, Norman D, Price DC, Newton TH. Metrizamide and radionuclide cisternography in communicating hydrocephalus. *Radiology*. 1979 Mar;130(3):681-6.

[49] W R Nitz, W G Bradley, Jr, A S Watanabe, R R Lee, B Burgoyne, R M O'Sullivan, M D Herbst. Flow dynamics of cerebrospinal fluid: assessment with phase- contrast velocity MR imaging performed with retrospective cardiac gating. *Radiology*, 1992.

[50] Grover T, Singer JR. NMR spin echo flow measurements. *J Appl Phys* 1971; 42:938-940.

[51] Edelman RR, Wedeen Vj, Davis KR, et al. Multiphasic MR imaging: a new method for direct imaging of pulsatile CSF flow. *Radiology* 1986; 161:779-783.

[52] Ridgway JP, Turnbull Lw, Smith MA. Demonstration of pulsatile cerebrospinal fluid flow using magnetic resonance phase imaging. *Br J Radio.* 1987; 60:423-427

[53] Battal B, Kocaoglu M, Bulakbasi N, Husmen G, Tuba Sanal H, Tayfun C. Cerebrospinal fluid flow imaging by using phase-contrast MR technique. *Br J Radiol*. 2011; 84(1004):758-765.

[54] Mascalchi M, Ciraolo L, Tanfani G, et al. Cardiac-gated phase MR imaging of aqueductal CSF flow. *Journal of Computer Assisted Tomography*. 1988;12(6):923-926.

[55] Enzmann DR, Pelc NJ. Normal flow patterns of intracranial and spianl fluid de- fined with Phase Contrast cine MR imaging. *Radiology*. 1991; 178:467-484.

[56] Freddy Ståhlberg, Jens Mogelvang, Carsten Thomsen, Bo Nordell, Max Stub- gaard, Anders Ericsson, Göran Sperber, Dan Greitz, Henrik Larsson, Ole Henriksen, Bertil Persson. A method for MR quantification of flow velocities in blood and CSF using interleaved gradient-echo pulse sequences, *Magnetic Resonance Imaging*. 1989; 655- 667.

[57] Patrick H. Luetmer, John Huston, Jonathan A. Friedman, Geoffrey R. Dixon, Ronald C. Petersen, Clifford R. Jack, Robyn L. McClelland, Michael J. Ebersold, Measurement of Cerebrospinal Fluid Flow at the Cerebral Aqueduct by Use of Phase Contrast Magnetic Resonance Imaging: Technique Validation and Utility in Diagnosing Idiopathic Normal Pressure Hydrocephalus, *Neurosurgery*. 2002; 534–543.

[58] Thalakotunage, Amila Sethaput, Thunyaseth. Quantification of CSF velocity through the narrowest point in aqueduct of sylvia for normal and normal pressure hydrocephalus patient by CFD analysis. *International Journal of Pharmacy and Pharmaceutical Sciences*. 2016.

[59] Enzmann DR, Pelc NJ. Normal flow patterns of intracranial and spinal cerebrospinal fluid defined with phase-contrast cine MR imaging. *Radiology*. 1991;178(2):467-474.

[60] Stadlbauer, A., Salomonowitz, E. Wilma van der Riet, Michael Buchfelder, Oliver Ganslandt. Insight into the patterns of cerebrospinal fluid flow in the human ventricular system using MR velocity mapping. *NeuroImage*. 2010; 42-5

[61] Stadlbauer A, Salomonowitz E, Brenneis C, et al. Magnetic resonance velocity mapping of 3D cerebrospinal fluid flow dynamics in hydrocephalus: preliminary results. *Eur Radiol*. 2012; 22(1):232-242.

[62] Algin O, Turkbey B. Evaluation of aqueductal stenosis by 3D sampling perfection with application-optimized contrasts using different flip angle evolutions sequence: preliminary results with 3T MR imaging. *AJNR Am J Neuroradiol*. 2012; 33(4):740-746.

[63] Matsumae M, Hirayama A, Atsumi H, Yatsushiro S, Kuroda K: Velocity and pressure gradients of cerebrospinal fluid assessed with magnetic resonance imaging. *J Neurosurg*. 2014; 120: 218–227.

[64] Hirayama A, Matsumae M, Yatsushiro S, Abdulla A, Atsumi H, Kuroda K: Visualization of pulsatile CSF motion around membrane-like structures with both 4D velocity mapping and Time-SLIP technique. *Magn Reson Med Sci.* 2015; 14: 263–273.

[65] Nowoslawska E, Gwizdala D, Baranska D, et al.: The oscillatory flow of the cerebrospinal fluid in the Sylvian aqueduct and the prepontine cistern measured with phase contrast MRI in children with hydrocephalus-a preliminary report. *Childs Nerv Syst* 2018; 34: 845–851.

[66] Shibukawa S, Miyati T, Niwa T, et al.: Time-spatial labeling inversion pulse (Time-SLIP) with pencil beam pulse: a selective labeling technique for observing cerebrospinal fluid flow dynamics. *Magn Reson Med Sci*, 2018; 17: 259–264.

[67] Wymer DT, Patel KP, Burke WF 3rd, Bhatia VK. Phase-Contrast MRI: Physics, Techniques, and Clinical Applications. *Radiographics*. 2020;40(1):122-140.

[68] Stankovic Z, Allen BD, Garcia J, Jarvis KB, Markl M. 4D flow imaging with MRI. Cardiovasc Diagn Ther 2014;4(2):173-192.

[69] Korbecki A, Zimny A, Podgórski P, Sąsiadek M, Bladowska J. Imaging of cerebrospinal fluid flow: fundamentals, techniques, and clinical applications of phase-contrast magnetic resonance imaging. *Pol J Radiol*. 2019; 84:e240-e250.

[70] Kapsalaki E, Svolos P, Tsougos I, Theodorou K, Fezoulidis I, Fountas KN. Quantification of normal CSF flow through the aqueduct using PC-cine MRI at 3T. *Acta Neurochir Suppl*. 2012; 113:39-42.

[71] Lee JH, Lee HK, Kim JK, Kim HJ, Park JK, Choi CG. CSF flow quantification of the cerebral aqueduct in normal volunteers using phase contrast cine MR imaging. *Korean J Radiol*. 2004; 5(2):81-86.

[72] Yoshida K, Takahashi H, Saijo M, et al. Phase-contrast MR studies of CSF flow rate in the cerebral aqueduct and cervical subarachnoid space with correlation-based segmentation. *Magn Reson Med Sci*. 2009; 8(3):91-100.

[73] Nitz, W R; Bradley, W G; Watanabe, A S; Lee, R R; Burgoyne, B; O'Sullivan, R M; Herbst, M D. Flow dynamics of cerebrospinal fluid: assessment with phase-contrast velocity MR imaging performed with retrospective cardiac gating. *Radiology*. 1992; 183(2), 395–405.

[74] Spraggins TA. Wireless retrospective gating: application to cine cardiac imaging. *Magn Reson Imaging*. 1990;8(6):675-681.

[75] Lenz GW, Haacke EM, White RD. Retrospective cardiac gating: a review of technical aspects and future directions. *Magn Reson Imaging*. 1989;7(5):445-455.

[76] Chinchali, A.P. Eddy Current Correction in PC-MRI: An Analysis of Local and Global Static Tissue Fitting Techniques. UCLA, 2018.

[77] Hugo Ferreira, Hugo & Ramalho, Joana. Basic Principles of Phase Contrast Magnetic Resonance Angiography (PC MRA) and MRV. *Vascular Imaging of the Central Nervous System.* 2013.

[78] Wentland AL, Wieben O, Korosec FR, Haughton VM. Accuracy and reproducibility of Phase Contrast MR imaging measurements for CSF flow. *Am. J. Neuroradiol*, 2010; 31:1331–36.

[79] Aletras AH, Ding S, Balaban RS, Wen H. DENSE: displacement encoding with stimulated echoes in cardiac functional MRI. *J Magn Reson*. 1999; 137(1):247-252.

[80] Soellinger, M., Rutz, A. K., Kozerke, S. and Boesig er, P., 3D cine displacement-encoded MRI of pulsatile brain motion. *Magn. Reson. Med*., 2009; 61: 153-162.

[81] Van Gelderen P, de Zwart JA, Starewicz P, Hinks RS, Duyn JH. Real-time shimming to compensate for respiration-induced B0 fluctuations. *Magn Reson Med*. 2007;57(2):362-368.

[82] Adams AL, Viergever MA, Luijten PR, Zwanenburg JJM. Validating faster DENSE measurements of cardiac-induced brain tissue expansion as a potential tool for investigating cerebral microvascular pulsations. *Neuroimage*. 2020;208:116466.

[83] Pahlavian, S. H., Oshinski, J., Zhong, X., Loth, F. Amini, R. Regional Quantification of Brain Tissue Strain Using Displacement-Encoding With Stimulated Echoes Magnetic Resonance Imaging. *J. Biomech. Eng*. 2018; 140, 081010.

[84] Adams, A. L., Kuijf, H. J., Viergever, M. A., Luijten, P. R. Zwanenburg, J. J.M. Quantifying cardiac-induced brain tissue expansion using DENSE. *NMR Biomed*. 2019, 32, e4050.

[85] Sloots, J. J., Adams, A. L., Luijten, P. R., Biessels, G. J. Zwanenburg, J. J.M. Unraveling cardiac and respiratory contributions to brain tissue motion using single shot 2D DENSE at 7T MRI. *ISMRM Proc*. 2018; 2, 368.

[86] Brittain JH, Hu BS, Wright GA, Meyer CH, Macovski A, Nishimura DG. Coronary angiography with magnetization prepared T2 contrast. *Magn Reson Med*. 1995 May; 33(5):689-96.

[87] D. Greitz, A. Franck & B. Nordell. On the Pulsatile Nature of Intracranial and Spinal CSF-Circulation Demonstrated by MR Imaging, *Acta Radiologica*. 1993; 34:4, 321-328.

[88] L. Howden, D. Giddings, H. Power, A. Aroussi, M. Vloeberghs, M. Garnett & D. Walker. Three-dimensional cerebrospinal fluid flow within the human ventricular system, *Computer Methods in Biomechanics and Biomedical Engineering*. 2008; 11:2, 123-133.

[89] O. Bale´dent, M.C. Henry-Feugeas and I. Idy-Peretti. Cerebrospinal fluiddynamics and relation with blood flow: a magnetic resonance study with semiautomated cerebrospinal fluid segmentation. *Invest.Radiol*. 2001; 37;368 – 377.

[90] R.K. Parkkola, M.E. Komu, T.M. Aarimaa, M.S. Alanen and C. Thomsen. Cerebrospinal fluid flow in children with normal and dilated ventricles studied by MR imaging. *Acta Radiol*. 2001; 42(1); 33 – 38.

[91] Loth, M.A. Yardimci and N. Alperin. Hydrodynamic modeling of cerebrospinal fluid motion within the spinal cavity. *J. Biomech.Eng*. 2001; 123(1); 71 – 79.

[92] Nett EJ, Johnson KM, Frydrychowicz A, et al. Four-dimensional phase contrast MRI with accelerated dual velocity encoding. *J Magn Reson Imaging*. 2012;35(6):1462-1471.

[93] Ha H, Kim GB, Kweon J, et al. Multi-VENC acquisition of four-dimensional phase-contrast MRI to improve precision of velocity field measurement. *Magn Reson Med*. 2016;75(5):1909-1919.

[94] Schnell S, Ansari SA, Wu C, et al. Accelerated dual-venc 4D flow MRI for neurovascular applications. *J Magn Reson Imaging*. 2017;46(1):102-114.

[95] Moersdorf R, Treutlein M, Kroeger JR, et al. Precision, reproducibility and applicability of an undersampled multi-venc 4D flow MRI sequence for the assessment of cardiac hemodynamics. *Magn Reson Imaging*. 2019;61:73-82.

[96] Park S, Chen L, Townsend J, Lee H, Feinberg DA. Simultaneous Multi-VENC and Simultaneous Multi-Slice Phase Contrast Magnetic Resonance Imaging. *IEEE Trans Med Imaging*. 2020;39(3):742-752.

Appendix

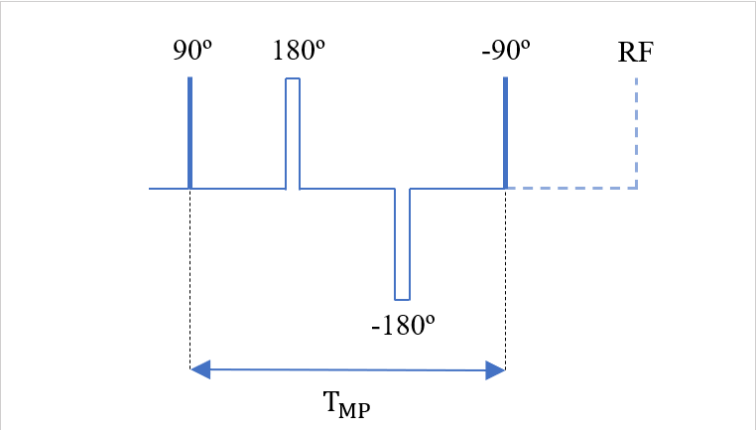

Figure A.1: T_2 prepared magnetization applied before the DENSE sequence.